平成２８年度　長岡技術科学大学

大学院研究科工学研究科　博士論文

耐環境用途に向けた複合酸化物およびその複合材料の材料設計と創製に関する研究

Design and Synthesis of Complex Oxide and Its Composites for Environmental Resistance Application

専攻　　材料工学

学籍番号　11507588

氏名　　NGUYEN SON THANH

指導教員　中山　忠親　准教授

(様式)

論　文　内　容　の 要　旨

氏　名　NGUYEN SON THANH

セラミック酸化物は、人類の発展に非常に重要な役割を有している。代表的な材料として、レンガは 1000 年以上前から建築・建設において使用されてきた。現在では、坩堝または鋳型を製造するための耐火物としてジルコニア（ZrO_2）やアルミナ（Al_2O_3）等、機械部品を保護するための被覆としてムライトが広く使用されている。この論文は、一般的な環境耐性セラミック酸化物の重要性のみではなく、それらが直面している問題についても検討し、耐環境材料として新規材料を発見する必要性を示した。

本研究では、酸化物分散強化型鋼内に分散している $Y_2Ti_2O_7$ が極めて高い安定性を有していることに着目し、当該材料が様々な用途に対して耐環境材料として優位性を有していることを明らかにしている。

本論文は、「耐環境用途に向けた複合酸化物およびその複合材料の材料設計と創製に関する研究」と題し、以下の 5 章より構成されている。

第 1 章の「Introduction and literature review」では、一般的な耐環境セラミック酸化物の重要性、直面している問題について述べ、酸化物分散強化型鋼内に分散している $Y_2Ti_2O_7$ が極めて高い安定性を有していることについて説明する。また、本論文の構成について説明している。

第 2 章の「$Y_2Ti_2O_7$ – a high corrosion-resistant ceramic 」では、まず固相反応及びホットプレス法を用いることで $Y_2Ti_2O_7$ 焼結体を合成した。合成した焼結体をアルミニウム（Al）ホイルで挟み、Al の融点以上の温度で加熱することで積層体を作製した。XRD の結果より、溶融 Al とセラミックスは反応しないことを確認した。更に、微細構造の観察および EDS の結果より、緻密化により $Y_2Ti_2O_7$ セラミックスの溶融金属耐食性が改善できることが明らかとなった。これらの結果は、$Y_2Ti_2O_7$ が坩堝と鋳造金型のための有望な材料であることを示唆している。

第 3 章の「Low thermal conductivity $Y_2Ti_2O_7$ – a candidate for thermal/environmental barrier coatings 」では、T/ EBC(Thermal/Environmental Barrier Coating)のための候補材料としての可能性を調査するために、ニッケル （Ni）又は SiC と $Y_2Ti_2O_7$ のセラミックマトリックス複合材料を合成した。複合材料は 25 MPa でホットプレス法より焼結した。そして、密度、ビッカース硬度及び破壊靭性などの複合材料の機械的特性を評価した。測定結果から、Ni や SiC のフィラーにより複合材料の破壊靭性が向上することが示された。微細構造の観察より、$Y_2Ti_2O_7$/Ni はイントラ/インターナノ複合材料であり、$Y_2Ti_2O_7$/SiC はネットワーク微細構造複合体の特性を有していることが明らかとなった。また、XRD と EDS 分析結果より、$Y_2Ti_2O_7$ は Ni に対して安定であることが示された。しかし、焼結後の複合材料でケイ酸塩が確認され、この反応のメカニズムとして焼結プロセス中に $Y_2Ti_2O_7$ と SiC が反応したことが原因と考えている。

第 4 章の「Fabrication of functionally graded $Y_2Ti_2O_7$/SiC composites 」では、まず溶液化学法を用い、SiC ナノファイバーの表面に対して Ni ナノ粒子のコーティングを行った。次いで、Ni-SiC ナノファイバーは、2-プロパノール溶媒及び PEI 分散剤を用いてボールミルにより製造された $Y_2Ti_2O_7$ のスラリーに分散させた。その後、スラリーをポリエチレンの型に注ぎ、磁場印加により Ni-SiC を配列させた。磁場印加後、成形体をアルゴン雰囲気中で常圧焼結した。作製した焼結体の断面観察

の結果より、Ni-SiC のナノファイバーが磁場方向に沿って整列され、$Y_2Ti_2O_7$ と SiC の間に凹凸界面が形成されたことが確認された。

第 5 章の「General conclusions」では、得られた結果から、$Y_2Ti_2O_7$ は高温で高い耐食性、低い熱伝導性、相安定性などの多くの優れた特性を有することが確認できた。Al_2O_3 やムライトや YSZ 等の既知の耐環境材料と比較すると、$Y_2Ti_2O_7$ は優秀な特性を示す。従って、$Y_2Ti_2O_7$ セラミック酸化物及びその複合材料は、坩堝や鋳型を鋳造するためだけでなく、T/EBC 及び他の多くの耐環境材料への応用も非常に有望な材料であると結論付けることができる。

Table of Contents

Chapter 1: Introduction and Literature Review

Abstract

Ceramic oxides have a very important role in the development of the mankind. For thousand years, bricks have been used in building and construction. Refractories like alumina (Al_2O_3), zirconia have been widely used to fabricate crucibles or casting molds. Mullite ($3Al_2O_3.2SiO_2$) has been employed to coat on and protect turbine engine's blades, etc. This chapter briefly reviews the importance of environmental-resistant ceramic oxides, as well as the challenges they are facing. Then, $Y_2Ti_2O_7$ is also introduced and explained why it is considered as a promising alternative material for environmental-resistant applications.

1.1. Development of environmental-resistant ceramic oxides, their importance and challenges

Ceramic oxides have a very important role in the development of the mankind. For thousands years, bricks have been used for building houses and many constructions. Refractories like alumina, zirconia have been widely used to fabricate crucibles or casting molds. Mullite, yttria stabilized zirconia (YSZ), have been employed as coating layers to protect turbine engine blades from hot-inlet gas. Comparing to metals and alloys, ceramic oxides usually possess excellent physical properties like chemical stability at higher temperature, high corrosion and high wear resistance, low thermal conductivity and low thermal expansion coefficient (CTE). Therefore, ceramic oxides and their composites have been widely used in severe environments, which are extremely hot (thousands degree Celsius), highly irradiated, and have highly chemical reactivity. This section reviews the roles and challenges of the so-called environmental-resistant ceramic oxides and their composites in many different applications.

1.1.1. Environmental-resistant ceramic oxides as crucible and casting mold

Investment casting has been a widely applied in manufacturing weapons, jewels, arts, turbine blades and many more industrial/scientific components (1). However, the corrosion of casting molds or crucibles, which occurs when these containers are exposed to molten metal or molten slag over a long period, annually carries an enormous cost to the manufacturing industry (2). To reduce this corrosion cost, many kinds of refractory materials have been used to manufacture containers or coat on their surface. Ceramics are particularly preferred than metal as coating or shell mold materials because they usually posses better corrosion, oxidation and wear resistance (3,4). Among ceramics for conventional shell molds and crucible, alumina is one of the most applied materials (4) because of its low-cost and inertness in molten metal like iron and nickel, owning to the chemical stability of its Al-O bond array (5). Kim *et al*. in their studies (6,7) demonstrated the thermal stability of Al_2O_3 against molten magnesium alloy at temperature lower than 600 °C. However, they also pointed out there was reaction obviously occurred between the ceramic and the alloy at higher temperatures (7). Previously, the investigation of Laurent et al. (8) revealed that Al_2O_3 possibly was attacked by molten aluminum. In another study, Fernandez and co-workers showed that when being exposed at 1500 °C with NiO and vanadium slag, Al_2O_3 reacted with the oxides and was diffused by metallic ions (Ni, Mg, Fe, and V) existing in the molten slag (9). There have been many materials suggested for substituting Al_2O_3, such as chromia (Cr_2O_3) or its combination with Al_2O_3, the chromia-alumina (Cr_2O_3-Al_2O_3) ceramic (10). However, Cr_2O_3 was observed to be attacked by aluminum alloys even at temperatures lower than 750 °C (4) and Cr_2O_3-Al_2O_3 was still damaged by molten slag and molten salt (10,11) (Fig. 1.1). Yttria (Y_2O_3) and magnesia (MgO) have been considered as most promising candidates because these oxides are very stable at high temperatures owning to their strongly negative standard free energy for the formation of oxides, an indicator for the suppression of

mold-metal reaction (7,12). It is also noteworthy to be noticed that, though Y_2O_3 is very expensive, it is more stable than MgO (7,12), and is the only one among investigated oxides which showed no reaction with magnesium melt (12).

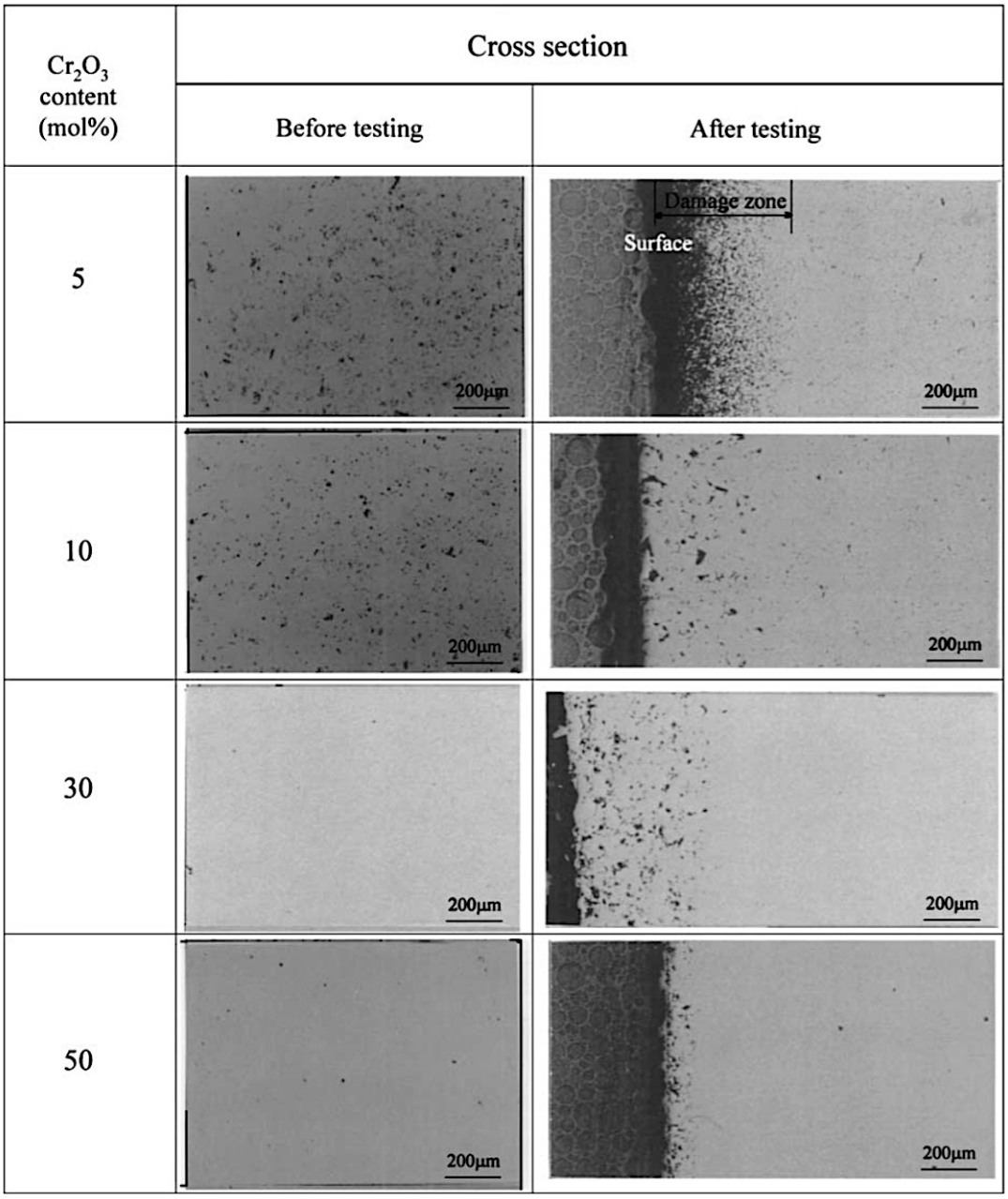

Fig. 1.1. Cross section of Cr_2O_3-Al_2O_3 ceramics (testing temperature: 900 °C) [11]

1.1.2. Environmental-resistant ceramic oxides as thermal/environmental barrier coating materials

The efficiency and core power of gas-turbine engines used in aircraft are directly related to the turbine inlet temperature, where a higher operation temperature provides better turbine performance (13,14). Thermal barrier coatings (TBC) have been introduced to protect nickel-based superalloy turbine components from hot inlet gas, enabling engines to operate at higher temperatures. Yttria-stabilized zirconia (YSZ) has been widely applied as a TBC because of its low thermal conductivity and chemical inertness (15–17). However, YSZ is considered to have reached its limit in terms of temperature capability, while superalloys cannot endure higher temperatures due to the low melting points of the metallic components (18,19). These limitations have encouraged explorations to find new materials for the hot sections of gas turbine engines.

With respect to substrate materials, ceramic matrix composites (CMCs) have attracted much interest because when compared to superalloys, their higher temperature capability and much lower density allow for reductions in fuel consumption (20,21). Among the CMCs, silicon carbide fiber/silicon carbide matrix (SiC_f/SiC_m) has been widely considered as the most promising for the components of next-generation aircraft gas turbine engines (22,23). When SiC is exposed to oxidative environments, it reacts with oxygen to form a protective SiO_2 layer, which in turn reacts with water vapor in hydrocarbon-rich inlet gas to create gaseous silicon hydroxides and leads to SiC recession (22,24). Therefore, it is a prerequisite to protect the SiC_f/SiC_m substrate from recession during the thousands of operation hours by the application of environmental barrier coatings (EBC). The first generation of EBC is a layer of mullite directly coated on SiC/SiC substrate. But SiO_2 is quickly vaporized at high temperature leaving only Al_2O_3 scale. Alumina in turn is readily spalled, therefore this EBC is able to provide a very short protection for the substrate (25). To avoid the volatilization of

SiO_2, a layer of YSZ is added on the mullite (26). However, the CTE mismatch between either YSZ/mullite and mullite/SiC leads to the appearance of cracks in their interfaces, as a result the delamination of the upper layers often occurs (27,28). In the third generation, YSZ is replaced by Barium–strontium aluminosilicate (BSAS) and a bond-coat layer of Si is added between mullite and SiC substrate, to reduce the CTE mismatch between layers (29). This multi-layered structure has proven to be effect in protect turbine blades at temperatures under 1000 °C. However, the low melting eutectics occur near 1300 °C limits the usage of this EBC at higher temperatures or lifetime longer than 1000 h (29) (Fig. 1.2.). Therefore, new materials for the top coat with low volatility and high temperature phase stability are required.

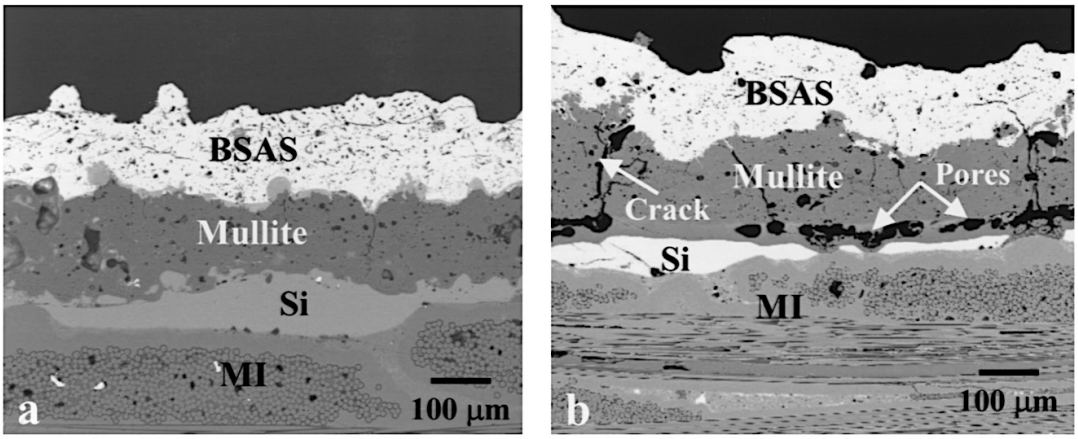

Fig.1.2. (a) and (b) Cross sections of Si/mullite/BSAS on SiC/SiC substrate after 1000 h in 90% H_2O–balance O_2 at 1300 °C with 1 h cycles; many cracks and pores can be observed [22]

There have been many candidates proposed for this position such as $Yb_2Si_2O_5$, Y_2SiO_5 (rare-earth monosilicates), or Y_2SiO_7 (rare-earth disilicate) but there is still no one can completely solve the problem. The monosilicates readily react with calcium-magnesium-aluminosilicate (CMAS) from inlet gas and generate unpredictable phases (Fig. 1.2), which are often detrimental to the mechanical properties of the coating (23,30). In the case of

$Y_2Si_2O_7$, although this disilicate has been already saturated and hence will not react with CMAS, its high thermal conductivity (31) does not assure a good thermal protection for the underneath layers. In general, the quest for a reliable material for EBC top coat is still an imperative mission.

1.1.3. Environmental-resistant ceramic nanocomposites, their designs and synthesis

Ceramic nanocomposites, which were pioneered by Niihara (32) in 1991, have strongly contributed into the development of super-tough and high-strength materials. Since then, there have been numerous researches on the fabrication and characterization of ceramic-based nanocomposites, with both ceramic and metallic fillers (33–36). However, in almost fabricated nanocomposites, the particulate/whisker/fiber second phases were homogeneously distributed within the ceramic matrix, therefore they are very useful in enhancing the properties of the entire composite, but not in a specific direction. On the other hand, functionally graded materials (FGM), which were also pioneered by Japanese scientists, more than three decades ago (37), is a class of advanced materials with varying properties over a changing dimension. The basic concept of FGM is to vary the composition of the composite in a specific direction, for instance top-down direction, to gradually change the properties of the composite for a specific purpose. Multilayered composites, having the same purpose with FGM but more simple in fabrication, are composed of many layers in which the adjacent layers are different in composition, but very close to each other in a certain property. Multilayered composites have been applied to fabricate armor, thermal/environmental barrier materials, etc. (23,38).

There are several methods to fabricate FGM or multilayered composites: plasma spraying, vapor deposition, electrophoretic deposition, etc. (39). However, all these methods are energy intensive, expensive, and in most cases only able to coat layer-by-layer on the

substrates. Because of the difference in thermal expansion between these layers, when the composites endure high temperatures over very long periods, the cracks appeared at the interface of layers and finally can cause the delamination of the layers. Convex-concave interface has been proposed to improve the adhesive bonding between the layers (40), but it is very expensive and complicated to fabricate convex-concave interface with conventional method like sputtering or vapor deposition. Therefore, a new method, inexpensive but effective, is necessary for fabricating convex-concave interface multilayered composites.

1.2. $Y_2Ti_2O_7$, a promising alternative material for environmental-resistant applications

Y_2O_3 has been widely used in fabrication of oxide-dispersion-strengthened (ODS) steels (41) for structural applications in nuclear fusion and fission reactor (42). The ODS steel can be manufactured by mechanical alloying Y_2O_3 powder with elemental powder (consisting of Fe, C, Cr, W, etc.) and additional titanium powder, followed by hot extrusion and machining as described in the work of Ukai *et al*. (43). The yttrium oxide is decomposed into yttrium (Y) and oxygen (O) during the mechanical alloying process (44,45), then re-precipitate with titanium to form more stable Y-Ti complex oxide (mainly yttrium titanate, or $Y_2Ti_2O_7$) (43,46). $Y_2Ti_2O_7$ is one of very first and most popular members of the $A_2B_2O_7$ family which have been synthesized and characterized. In 1978, Uematsu *et al*. investigated and reported the electrical transport properties of $Y_2Ti_2O_7$ for the first time (47). Since then, many scientists have studied on the electrical (48,49), thermal (48,50) and mechanical properties (51) of this ceramic oxide. As a member of the $A_2B_2O_7$ family (where A-site and B-site are 3^+ and 4^+ cations, respectively), $Y_2Ti_2O_7$ has pyrochlore structure (Fig. 1.3), whose unit cell is very similar to that of fluorite-structure, except the absence of one anion site (52,53). The fluorite structures, e.g. ZrO_2 or UO_2, have been demonstrated that especially stable under radiation environment, because they are almost unsusceptible to radiation-induced

amorphization (54,55). Under irradiation conditions, pyrochlore compositions can be disordered to the defect-fluorite structure, which is more radiation tolerant (56).

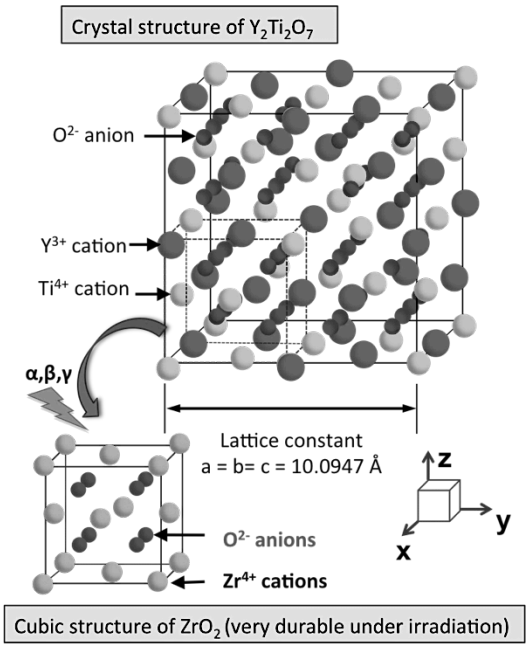

Fig. 1.3. Crystal structures of $Y_2Ti_2O_7$ and ZrO_2

There have been evidences that the introduction of Y_2O_3 nano-particles not only helped to increase the radiation resistance, but also enhanced the ductibility, creep rupture and high-temperature strength of the ODS steels (46,57). On the other hand, some composition analysis also indicated the main phase of precipitates in ODS steel is $Y_2Ti_2O_7$ (41,58). In 2013, Stan and co-workers observed the mesoscopic interfaces between $Y_2Ti_2O_7$ crystal wafer substrate and Fe grains epitaxially grown on it at 800 °C by electron beam and concluded that the interfaces are atomically clean with no significant transition layer (59). These findings suggest that the $Y_2Ti_2O_7$ oxide might not dissolve in and react with molten metal in the steel matrix (Fig. 1.4), even after heated at elevated temperature as high as 1150 °C (43). From this interesting point, it is reasonable to deduce that $Y_2Ti_2O_7$ oxide has excellent thermal and chemical stability against molten metal. Recently, Japanese scientists have invented a composite of $Y_2Ti_2O_7$ and $MgAl_2O_4$ which possesses very excellent chemical

stability, heat reflectance and sufficient corrosion resistance against molten alumina and aluminum alloys (60). However, the report did not give a full explanation about the molten metal corrosion resistance of the composite. The mechanism of corrosion resistance of $Y_2Ti_2O_7$, therefore, is still a question need to be answered.

When it comes to the candidate for T/EBC, it should be noticed that both conventional TBC and EBC are multilayered structures composed of bond coat, oxygen barrier, and top coat layers, in which the top coat is the most important and decisive component with respect to the performance of the structures. The following three criteria are most important for selecting candidates top coat materials: chemical stability at high temperature, low thermal conductivity, and a coefficient of thermal expansion (CTE) that matches that of the substrate to avoid cracking between the layers (18,23,61). Patrivia et al. (62) has demonstrated that the $Y_2Ti_2O_7$ pyrochlore has high chemical stability at high temperature . The CTE of $Y_2Ti_2O_7$ is reported as 8.36×10^{-6} K^{-1} (63), which is lower than that of YSZ (11×10^{-6} K^{-1}) (15), and closer to that of SiC (4×10^{-6} K^{-1}) (64). In addition, although there has been no report on the experimental thermal conductivity of monolithic $Y_2Ti_2O_7$ at high temperature, the published thermal conductivities of other pyrochlores such as $La_2Zr_2O_7$ (1.6 W m^{-1} K^{-1}) (65) and $Nd_2Zr_2O_7$ (1.3 W m^{-1} K^{-1}) (66) are much lower than that of YSZ (2.3 W m^{-1} K^{-1}) (15). Therefore, it is rational to predict that $Y_2Ti_2O_7$ also has lower thermal conductivity than YSZ. In summary, $Y_2Ti_2O_7$ may satisfy all of the requirements for a promising T/EBC candidate material.

1.3. Purpose of this research and the structure of this thesis

As mentioned in the above sections, it is necessary to find a new material that has high corrosion resistance, high-temperature phase stability, low thermal conductivity, and proper thermal expansion coefficient for environmental-resistant applications like crucible, casting

molds, thermal/environmental barrier coatings, etc. The main purpose of this study is to synthesize and sinter $Y_2Ti_2O_7$, then to extensively investigate its mechanical and thermal properties, in order to examine its applicability as a material for these applications. In addition, an effective method to fabricate convex-concave interface multilayered composites, which is considered to be beneficial to the adhesive bonding between the layers, is also an objective of this research.

In this thesis, those objectives are examined and answered, respectively. The composition of this thesis, and the contents in each chapter are presented as follows,

Chapter 1, Introduction and literature review, describes the roles and challenges of environmental-resistant ceramic oxides, introduces $Y_2Ti_2O_7$ as a promising alternative materials, and explains the purposes of this research.

Chapter 2, $Y_2Ti_2O_7$ - a high corrosion-resistant ceramic, describes the sintering of $Y_2Ti_2O_7$ discs from Y_2O_3 and TiO_2 by solid-state reaction and hot-pressing method, the densification of the sintered discs by hot-isostatic-pressing (HIP), the fabrication of $Y_2Ti_2O_7$ sandwich with aluminum (Al) foils. The reaction between the molten Al and the ceramics will be investigated by X-ray diffraction analysis, and the resistance of $Y_2Ti_2O_7$ ceramics against molten-metal penetration will be evaluated according to micro-structural observation and composition analysis on the cross-sections of the sandwiches.

Chapter 3, Low thermal conductivity $Y_2Ti_2O_7$ - a candidate for thermal/environmental barrier coatings, explains the fabrication of $Y_2Ti_2O_7$/Ni and $Y_2Ti_2O_7$/SiC nanocomposites. The mechanical properties of the composites including bulk density, Vickers hardness, and fracture toughness will be investigated. Microstructural observations, X-ray diffraction, and energy dispersive X-ray spectroscopy analysis will be conducted to investigate the chemical reactivity of $Y_2Ti_2O_7$ with Ni and SiC during the synthesis process.

Chapter 4, Fabrication of functionally graded $Y_2Ti_2O_7$/SiC composites, describes a new method to fabricate a composite of $Y_2Ti_2O_7$ and SiC with convex-concave interface. The method will combine slurry casting and magnetic field inducement techniques to develop a convex-concave interface structure. The structure is indented with Vickers tip to test the bonding at the interface of two layers. The analysis results are used to evaluate the delamination resistance of the layers in the composites.

Chapter 5, General conclusions, based on the obtained results, the applicability of $Y_2Ti_2O_7$ for different environmental-resistant applications is evaluated and summarized.

Chapter 2: $Y_2Ti_2O_7$ - a high corrosion-resistant ceramic

Abstract

In this chapter, ceramic discs of $Y_2Ti_2O_7$ were firstly sintered from Y_2O_3 and TiO_2 by solid-state reaction and hot-pressing method, and then densified by Hot-isostatic-pressing (HIP) before being employed to fabricate sandwiched structures with aluminum (Al) foils. The phase identification by X-ray diffraction confirmed no reaction between the molten Al and the ceramics, while the micro-structural observation and energy dispersive X-ray spectroscopy results revealed that the densification has improved the resistance of $Y_2Ti_2O_7$ ceramics against molten-metal penetration. The result of this chapter should be good reference data for designing crucible and casting molds.

2.1. Introduction

Corrosion of refractories and ceramics is a complex phenomenon that involves different mechanisms, such as dissolution, invasive penetration and chemical reaction. While the chemical stability of the refractory can be enhanced by selecting appropriate materials, its penetration-dissolution resistance is mostly affected by its structural porosity (67). As Gogotsi and Lavrenko pointed out, corrosion resistance in liquid media as well as in other environments depends on the density and purity of the bulk sample, the lower the density, the lower the corrosion resistance (68). In 2011, He *et al.* were successful in sintering $Y_2Ti_2O_7$ ceramics by hot-pressing method,(51) however, the sintered sample was not fully dense (bulk density < 99.5%) and hence probably be further densified for the use as a corrosion-resistant structural ceramics (67). In addition, the relationship between here have no many reports discussing on the relationship between the conditions of fabrication process (particle size, sintering pressure) and the mechanical properties of the $Y_2Ti_2O_7$ ceramics (flexural strength, hardness, density, porosity, etc.), that may have an influence on its corrosion resistance.

In this chapter, the mechanical properties of $Y_2Ti_2O_7$ ceramics are modified by controlling both the particle size of raw materials and the pressure of sintering process, and by the densification of sintered sample using hot isostatic pressing method; It is shown that the modifications improve the mechanical properties and the corrosion resistance of $Y_2Ti_2O_7$; In addition, the mechanism of the resistance of $Y_2Ti_2O_7$ against the penetration of molten metal is also discussed. The purpose of this chapter is to investigate the applicability of $Y_2Ti_2O_7$ as a candidate material for molten-metal corrosion resistant containers.

2.2. Experimental Procedure

2.2.1. Starting materials and sintering of $Y_2Ti_2O_7$ ceramics

Anatase TiO_2 (Sigma Aldrich Corp.) and Y_2O_3 (Shin-Etsu Chemical Co., Ltd.) were chosen as the starting materials to synthesize the $Y_2Ti_2O_7$ ceramics. The powder blend (Y_2O_3:TiO_2 molar ratio = 1:2) was ball-milled in anhydrous ethanol for 24 h followed by evaporation to extract the solvent and drying in an air oven at 80 °C, then dry ball-milled for 12 h. After that, the blend was calcined at 1200 °C for 5 h to facilitate the reaction between Y_2O_3 and TiO_2 to form $Y_2Ti_2O_7$. Then, the $Y_2Ti_2O_7$ powder was dry ball-milled for 12 h and sieved to break up agglomerates. Finally, the as-synthesized powder was sintered in a gas-pressure-sintering furnace (FVPHP-R-5, FRET-18, Fuji Dempa Kogyo Co., Ltd.) by hot uniaxial pressing, at different pressures (0 to 25 MPa), 1500 °C for 1 h, in argon (Ar) to form $Y_2Ti_2O_7$ ceramics disc (Ø = 20 mm). There are totally 6 types of ceramic discs, each of them was sintered at a designated pressure (0, 5, 10, 15, 20, and 25 MPa). For flexural strength measurement, larger discs (Ø = 44 mm) were also sintered by hot-pressing with the same conditions.

To further improve the mechanical properties of $Y_2Ti_2O_7$ ceramics, the as-synthesized $Y_2Ti_2O_7$ powder was pulverized to the finer one by mixing it with ethanol and ZrO_2 beads (30

μm) and rotating for 1 h at 3000 rpm in an ultra-fine grinding mill (Ultra Apex Mill, Kotobuki Industries Co., Ltd.). The morphology of $Y_2Ti_2O_7$ particles, before and after the beads-milling process, was observed by a transmission electron microscope (TEM) (JEM-2000FX, JEOL Ltd.) The bulk sample of pulverized $Y_2Ti_2O_7$ was also sintered by the same method followed by tests to measure the mechanical properties, in comparison with those of the sample sintered directly from as-synthesized $Y_2Ti_2O_7$ powder.

Bulk density of fabricated ceramics was measured in high purity toluene by the Archimedes method. Phases of $Y_2Ti_2O_7$ powders, before and after the beads-milling, were identified using an X-ray diffractometer (RINT 2500PC, Rigaku Corp.). The microstructure and porosity of samples were studied using a tabletop scanning electron microscope (TM-3000, Hitachi High-Technologies Corp.). For observation, the as-sintered and polished samples were thermally etched at 1300 °C for 1 h, before scanning electron microscopy.

The Vickers hardness H_V was measured according to Japanese Industrial Standard (JIS) R1610 by a hardness testing machine (HV-100, Mitutoyo Corp.) at different loads with a dwell time of 15 s. The flexural strength of as-sintered ceramic was tested according to JIS R1601. For measurement, sintered discs (Ø = 44 mm) were cut into specimens (36 × 4 × 3 mm) and measured using a four-point flexural strength testing machine (MODEL-1311 VRW, Aikoh Engineering Co., Ltd.), outer and inner spans are L_o = 30 and L_i = 10 mm, respectively (see Fig. 2.4a).

2.2.2. Densification of $Y_2Ti_2O_7$ ceramics and fabrication of $Y_2Ti_2O_7$/Al sandwiches

The as-sintered ceramic discs were pressed under high pressure of 80 MPa, at 1300 °C for 1h, in Ar atmosphere by a lab-scale Hot-isostatic-pressing (HIP) unit (O2-Dr.HIP, Kobe Steel Ltd.) to further enhance their properties. Because of the sample size limitation of the heating chamber, only ceramic discs with 20 mm in diameter were used in this experiment.

The $Y_2Ti_2O_7$ ceramic discs were used to fabricate some ceramic-metal sandwiches, in order to examine their corrosion resistance of $Y_2Ti_2O_7$ ceramics against molten metal. For making a sandwich, at first both surfaces of $Y_2Ti_2O_7$ ceramic discs were grinded and polished until 5 μm of roughness, then they were used to compact round-shaped laminates which were cut from aluminum (Al) foils (11μm of thickness). The sandwich was then put into a vacuum chamber and heated in Ar atmosphere without applying pressure, at high temperatures for 1 h. Figure 2.1a shows the schematic illustration of this experiment, while Figure 2.1b shows optical photograph of an $Y_2Ti_2O_7$ disc (left), an Al laminate (center) and a fabricated sandwich (right). The sandwich consists of two black ceramic discs at top and bottom, and a thin white layer of Al, which is compacted in between them.

Three types of $Y_2Ti_2O_7$-Al-$Y_2Ti_2O_7$ sandwiches heated at 560 °C, 660 °C (melting point of Al) and 800 °C, are denoted as S560, S660 and S800, respectively. $Y_2Ti_2O_7$ discs processed with HIP were also used to fabricate sandwich at 800 °C, denoted as S800H, in order to examine the effect of densification on the corrosion resistance of $Y_2Ti_2O_7$ ceramics to molten-metal. Table 2.1 summarizes all four types of sandwiches and their corresponding synthesis conditions.

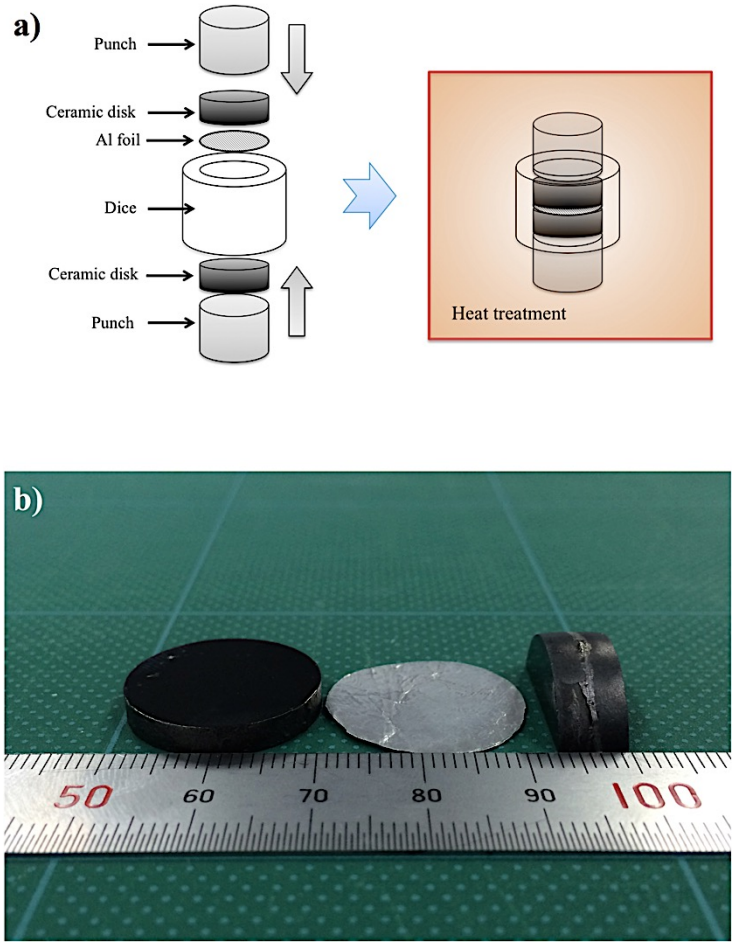

Fig. 2.1. Experiment of synthesizing $Y_2Ti_2O_7$/Al sandwich: (a) schematic illustration of the experiment, (b) optical photograph of a $Y_2Ti_2O_7$ disc (left), an Al foil (center) and a fabricated sandwich (right). The sandwich was cut in half and placed vertically to show the Al thin layer, which is gray and compacted in between two black $Y_2Ti_2O_7$ thick layers.

Table 2.1. Summary of sandwiches and corresponding synthesis conditions

Sandwich	Synthesis conditions				
	Heating temperature (°C)	Time (h)	Gas	Al foils	$Y_2Ti_2O_7$
S560	560	1	Ar	11 µm-thick	no HIP
S660	660				no HIP
S800	800				no HIP
S800H	800				HIP

2.2.3. Phase identification and elemental analysis

The fabricated sandwiches were brought into characterization to investigate the reaction between molten Al and sintered $Y_2Ti_2O_7$ as well as the penetration of the former into the latter. The sandwich was firstly cut into cross-sections and fixed onto a holder before brought to X-Ray diffraction (XRD). The position of the holder was gradually changed from time to time until the X-rays beam precisely diffracting on the interface region of Al and $Y_2Ti_2O_7$. The cross-section was then also observed and elemental analyzed using a field-emission scanning electron microscope (FE-SEM) equipped with energy dispersive X-ray spectroscopy (EDS) (JSM-6700F, JEOL Ltd.) in order to examine the penetration of metallic particles into the as-sintered ceramics. For the accuracy of the EDS results, only smooth areas on the sample surface were selected for the analysis to guarantee relative error smaller than 2%.

2.2. Results and Discussion

2.3.1. Mechanical properties of sintered ceramics

In this chapter, the mechanical properties of $Y_2Ti_2O_7$ ceramics was controlled by varying the pressure of the sintering process and the particles size of $Y_2Ti_2O_7$ powder. The dependencies of mechanical properties on both sintering pressure and particle size are discussed as follows:

a) Sintering pressure dependence

The $Y_2Ti_2O_7$ ceramic discs sintered at different pressures (0 to 25 MPa) were cut into cross-section to study their porosity by SEM observation. The micrographs in Figure 2.2 revealed that the quantity and size of pores inside the sintered ceramics decrease with the increasing of pressure. In the case of ceramic sintered without pressure (Fig. 2.2a), although some big grains can be seen, the fact that there are abundance of pores between the small

grains revealed that sintering pressure was not adequate for powder particles fusing together to form bigger and solid grains. When the powder was pressed under 5 MPa, the grains were developed to denser structures as shown in Figure 2.2b. Although there are some big pores between the grains, it is confirmed that the number of pores was also decreased considerably. When being applied under higher pressures (10, 15 MPa), the sintered ceramic can obtain further dense structure, with less and smaller pores (Fig. 2.2c, Fig. 2.2d). The ceramics sintered under 20 and 25 MPa show very dense structure, with very few and small pores (Fig. 2.2e, Fig. 2.2f). The relation between sintering pressure and density of ceramics is verified by bulk density measurements, whose results are shown in Figure 2.3 and summarized in Table 2.2. The bulk density of pressureless sintered ceramic (0 MPa) is 89.71% of 4.98 g cm^{-3} (the theoretical density of $Y_2Ti_2O_7$), much lower than 95.40 % of the pressure sintered ones (5 MPa), reflecting the difference of porous and dense structure shown in Fig. 2. Among pressure sintered ceramics, when the sintering pressure was gradually increased from 5 to 25 MPa, the bulk density also increased, very slightly but steadily, from 95.4 % to 98.88%. These data suggests that if we can increase the sintering pressure to be higher, a super full dense ceramic can be obtained. However, because of the limitation of the hot-press system, 25 MPa is the highest pressure can be applied. To further densify the ceramics, other sintering techniques like hot-isostatic-pressing (HIP) should be used. The densification of $Y_2Ti_2O_7$ ceramics using HIP will be discussed in later part of this section.

In addition to bulk density, Vickers hardness of the ceramics was also tested to show the effect of sintering pressure on mechanical properties of the sintered products. The tested results show a hardness-pressure relation that is quite similar to the density-pressure ones. While the non-pressure sintered sample has very low hardness (1.58 GPa), those of the

pressure sintered ones are much higher (9.73 to 10.62 GPa), showing a gradual increase with increasing pressure (see Fig. 2.3).

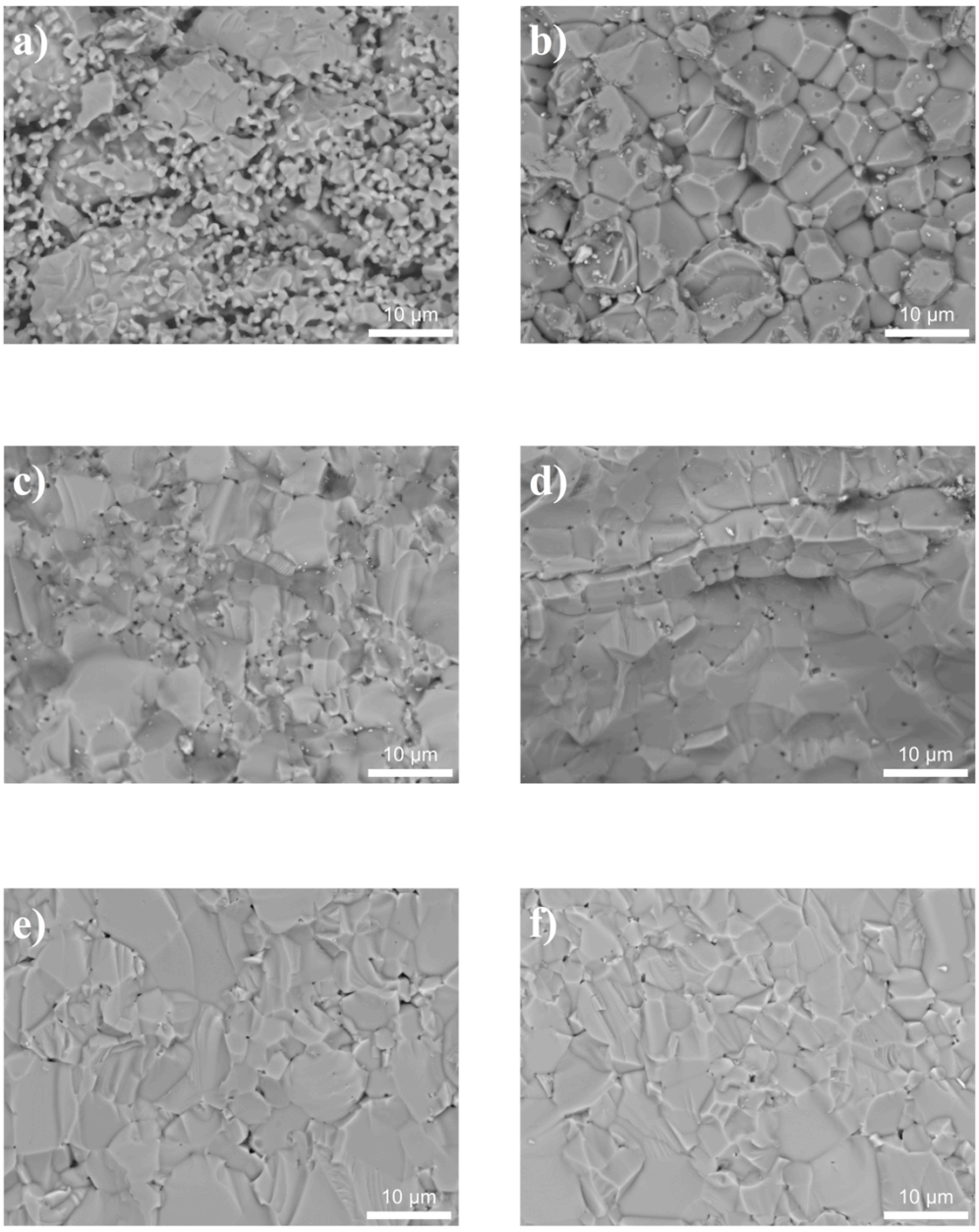

Fig. 2.2. SEM cross-sectional micrographs of $Y_2Ti_2O_7$ ceramics, sintered at different pressure: (a) 0 MPa, (b) 5 MPa, (c) 10 MPa, (d) 15 MPa, (e) 20 MPa, (f) 25 MPa.

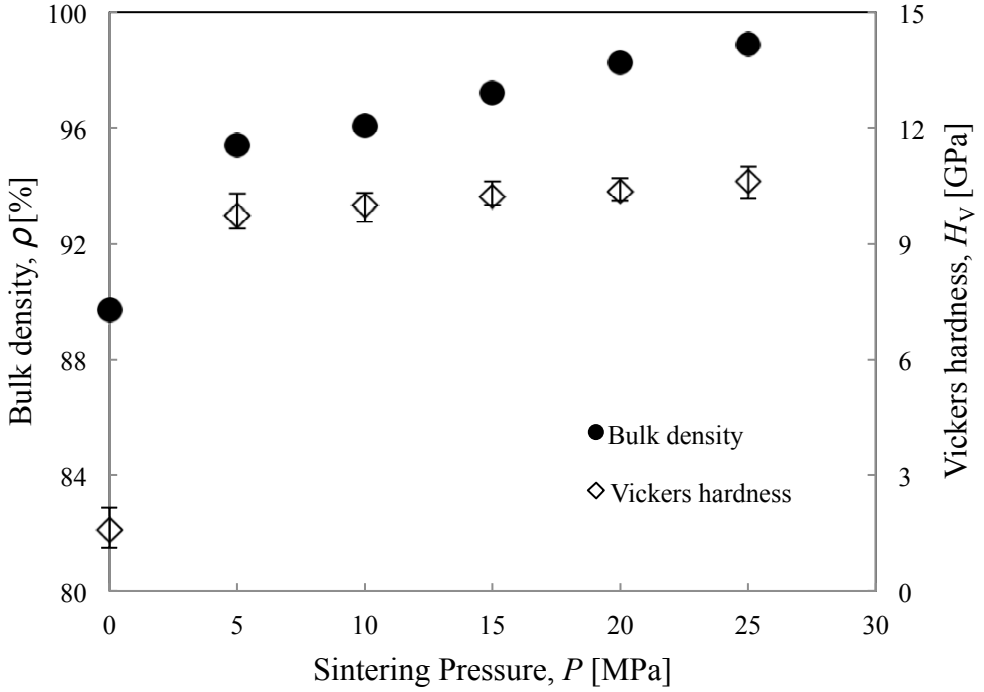

Fig 2.3. Bulk density and Vickers hardness of $Y_2Ti_2O_7$ as a function of sintering pressure

According to Rice (69), ceramic materials have a tendency to alternate the original fracture path with the new ones which propagate through more porous area , provided that the new path stays as close as possible to being approximately normal to the applied stress. This means that in the case of more porous materials, less energy is required for a crack propagating through a specimen to fracture it. In other words, the denser ceramic has more ability to resist rupture under stress. The flexural strength of the sintered ceramics was also tested to verify this inference. In this work, the four-point test method is selected instead of the three-point one because it is considered to be more appropriate for brittle material like $Y_2Ti_2O_7$ ceramic. The advantage of distributing the load over the inner span, rather than only focusing on the contact location as in three-point method, helps to preventing the specimen from deteriorating prematurely and therefore more reliable results can be obtained. The variation of flexural strength as a function of sintering pressure is presented in Figure 2.4b. When the sintering pressure gradually increase from 0 to 25 MPa, the flexural strength also

increased from 50 MPa to 206 MPa. From this result and the variation of bulk density that mentioned above, it can be concluded that the denser sintered ceramic has higher flexural strength.

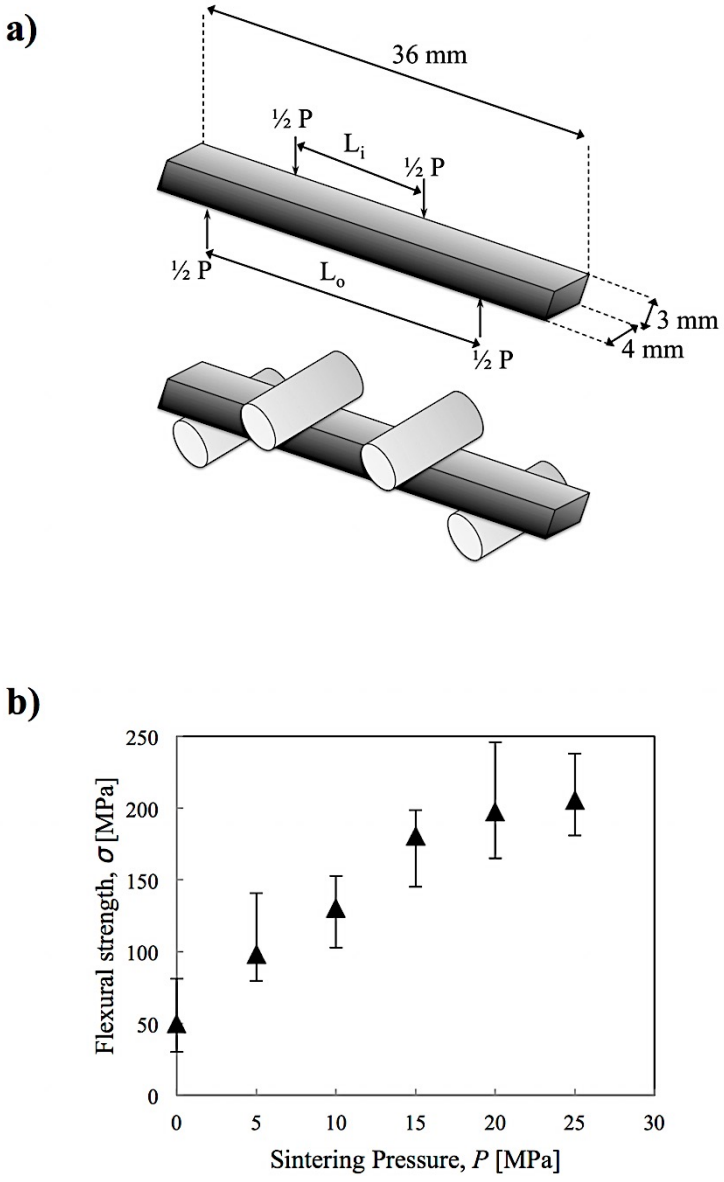

Fig. 4. Flexural strength test of $Y_2Ti_2O_7$ ceramics: (a) measurement of test specimens, and (b) sintering pressure dependence of flexural strength.

Table 2.2. Mechanical properties of sintered ceramics

$Y_2Ti_2O_7$ ceramic	ρ, %	H_V, GPa (9.8 N)	σ, MPa	Reference
no beads-mill, no HIP, Ø = 44 mm				
P = 0 MPa	$89.71^{+0.65}_{-0.33}$	$1.58^{+0.58}_{-0.46}$	50^{+31}_{-20}	This study
P = 5 MPa	$95.40^{+0.07}_{-0.04}$	$9.73^{+0.57}_{-0.33}$	99^{+42}_{-19}	This study
P = 10 MPa	$96.07^{+0.3}_{-0.48}$	$9.99^{+0.33}_{-0.41}$	131^{+22}_{-28}	This study
P = 15 MPa	$97.2^{+0.08}_{-0.15}$	$10.23^{+0.39}_{-0.24}$	181^{+18}_{-36}	This study
P = 20 MPa	$98.25^{+0.2}_{-0.22}$	$10.35^{+0.36}_{-0.24}$	198^{+48}_{-33}	This study
P = 25 MPa	$98.88^{+0.06}_{-0.06}$	$10.62^{+0.39}_{-0.45}$	206^{+32}_{-25}	This study
	99.39	$12.1^{+0.1}_{-0.1}$	206^{+33}_{-33}	He *et al.*[51]
no beads-mill, no HIP, Ø = 20 mm				
P = 25 MPa	$97.23^{+0.01}_{-0.01}$	$9.96^{+0.71}_{-0.36}$		This study
beads-mill, no HIP, Ø = 20 mm				
P = 25 MPa	$98.59^{+0.9}_{-0.14}$	$11.03^{+0.73}_{-0.77}$		This study
beads-mill, HIP, Ø = 20 mm				
P = 80 MPa	$99.87^{+0.08}_{-0.13}$	$12.21^{+0.42}_{-0.46}$		This study

b) Particle size dependence

In present chapter, in addition to the sintering pressure dependence, the relationship between the particle size and the mechanical properties was also investigated. The particle size of $Y_2Ti_2O_7$ powder can be changed by using starting materials (Y_2O_3 and TiO_2) with smaller or bigger particle size, however, the difference in starting materials composition can cause some minor but complicated variations in mechanical properties test results. To avoid that, this research used the same synthesized $Y_2Ti_2O_7$ powder but reduced its particle size by beads milling it with ZrO_2 micro-beads. Figure 2.5a shows a morphology of a ZrO_2 bead with a diameter of 30 μm, surrounded by $Y_2Ti_2O_7$ tiny particles. Very similar XRD patterns of as-synthesized and beads-milled powders shown in Figure 2.5b indicates that both powders are $Y_2Ti_2O_7$ single phase and there has been no contamination of ZrO_2 or other impurity phases

into the beads-milled powder. The TEM micrographs ((Fig. 2.5c and Fig. 2.5d) reveal that comparing to as-synthesized $Y_2Ti_2O_7$ powder, the particle size of the $Y_2Ti_2O_7$ powder after the beads-milling has been reduced, as evidenced by the more frequent appearance of small and medium particles. The particle size distributions of these two powders (Fig. 2.5e and Fig. 2.5f) expose that after the beads-mill process, the average particle diameter (D_{50}) of $Y_2Ti_2O_7$ powder is 159 nm, equal to 81.5% of that the unprocessed powder (D_{50} = 195 nm). Though the particle size was not reduced significantly due to the likelihood that many small $Y_2Ti_2O_7$ particles had been hidden in the voids between big ZrO_2 beads during the milling process, it can be realized that particles in the beads-milled powder are more similar to each other in size. This has been considered as an important aspect when sintering fine ceramics, because it helps to develop grains more uniformly and to reduce the quantity of pores between grains caused by the difference in size of grains. This effect can be verified by observing the microstructure of the thermally etched surfaces of the two types of $Y_2Ti_2O_7$ ceramics. Though there are not many differences in grain size, it is obvious that pores and cracks in $Y_2Ti_2O_7$ ceramic sintered from the as-synthesized powder (see Fig. 2.6a) are more than those in the one sintered from the beads-milled powder (Fig. 2.6b). The ceramic sintered from pulverized powder also posses the higher bulk density and Vickers hardness, as displayed in Figure 2.7. It is considered that the denser ceramic with fewer and smaller pores is less susceptible to Vickers indenter tip, thereby yielding a higher hardness value.

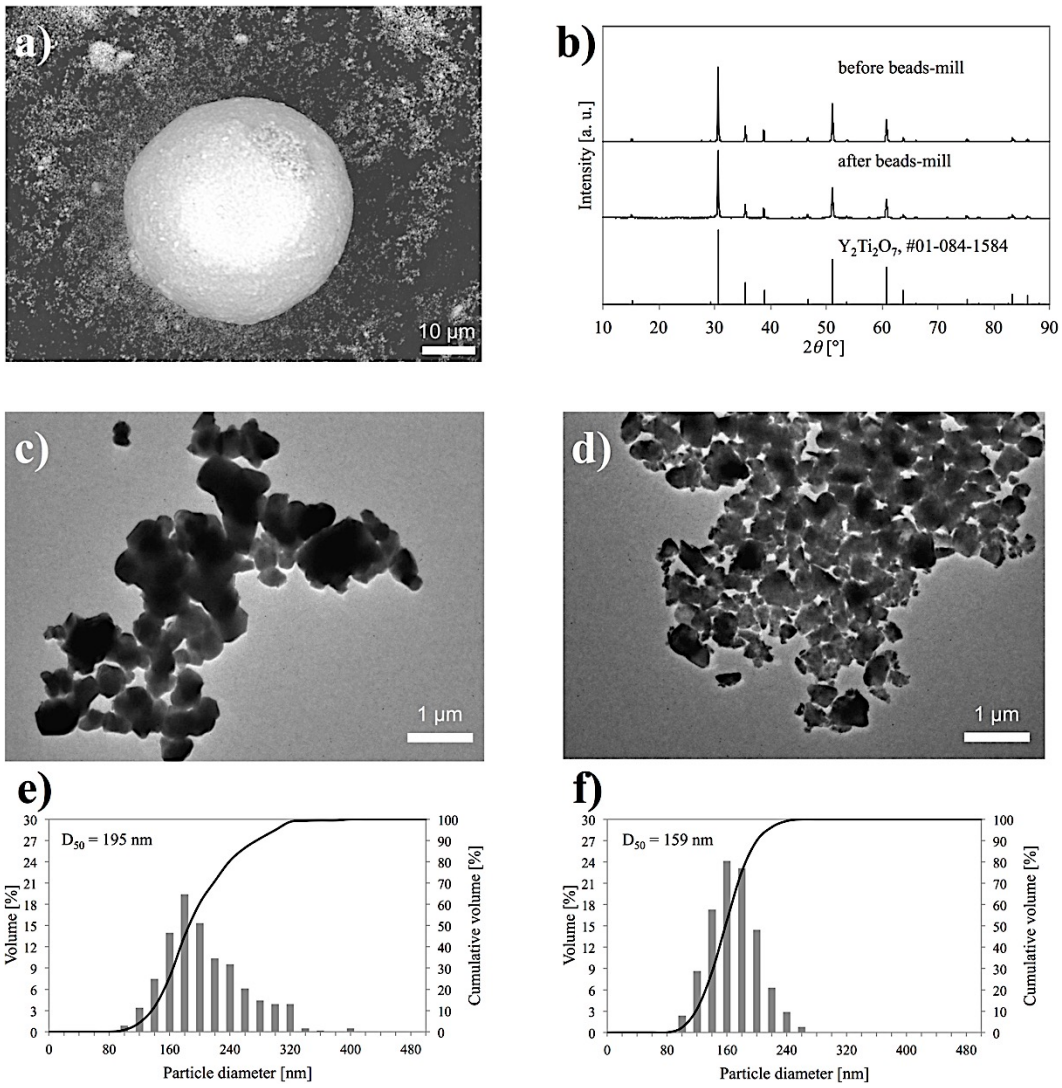

Fig. 2.5. Beads-mill process of $Y_2Ti_2O_7$ powder: (a) SEM micrograph of ZrO_2 beads and original powder, (b) XRD pattern of $Y_2Ti_2O_7$ powder, before and after beads-mill process, (c) TEM micrographs of Y2Ti2O7 particles before beads-mill process, (d) TEM micrographs of $Y_2Ti_2O_7$ particles after beads-mill process, (e) and (f) Particle size distribution of $Y_2Ti_2O_7$ before and after beads-mill process.

The mechanical properties including bulk density, flexural strength and Vickers hardness of the sintered ceramics are summarized in Table 2.2. These results are comparable to the works of He *et al.*(51).

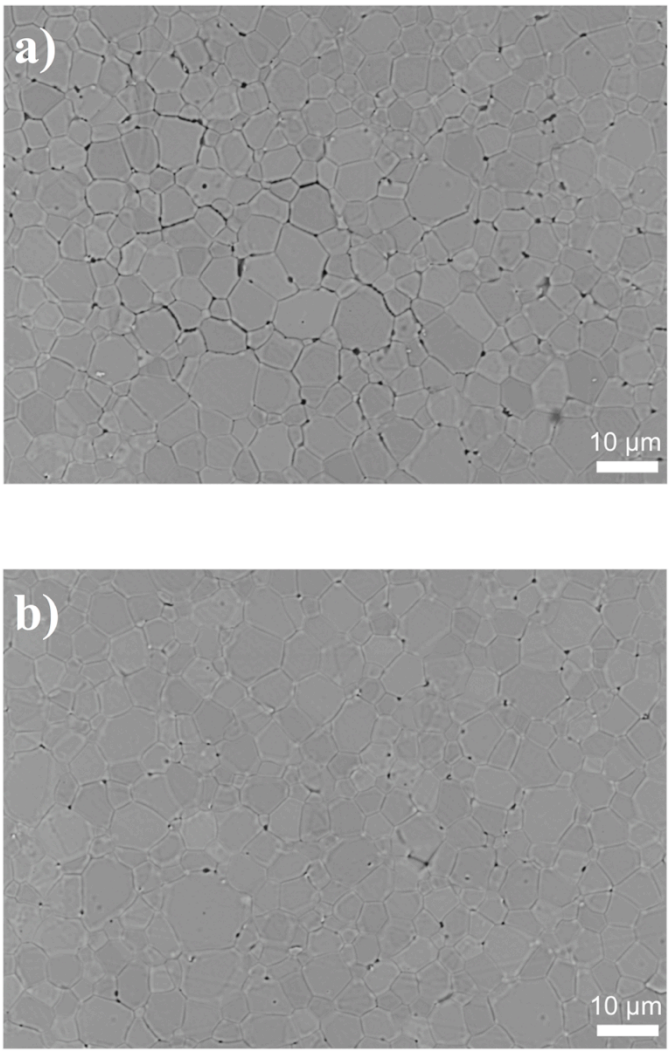

Fig. 2.6. SEM micrographs of ceramics, sintered from: (a) as-synthesized $Y_2Ti_2O_7$, and (b) beads-milled $Y_2Ti_2O_7$.

It should be noticed that the ceramic discs which were used for the mechanical tests reported in Figure 2.6 are 20 mm in diameter, while the ones previously mentioned in Figure 2.3 and Figure 2.4 are 44 mm in diameter. Though they were sintered at the same conditions (25 MPa, 1500 °C, Ar, 1h), the dissimilarity in their diameter can lead to small differences in the test results. This is because in uniaxial hot press sintering, the density is distributed unevenly from the center to the periphery of the ceramic discs. In the case of 20 mm ceramic discs, the whole disc was brought to bulk density measurement. However, in the case of

ceramic discs with 44 mm diameter, which is bigger than the weighing pan used for the bulk density measurements, they were cut into parts for the tests. The center parts were used for flexural strength measurement, while the periphery ones were used for density and hardness tests. Consequently, the measured density and hardness of 20-mm-diameter discs are slightly different from those of 44-mm-diameter-ones.

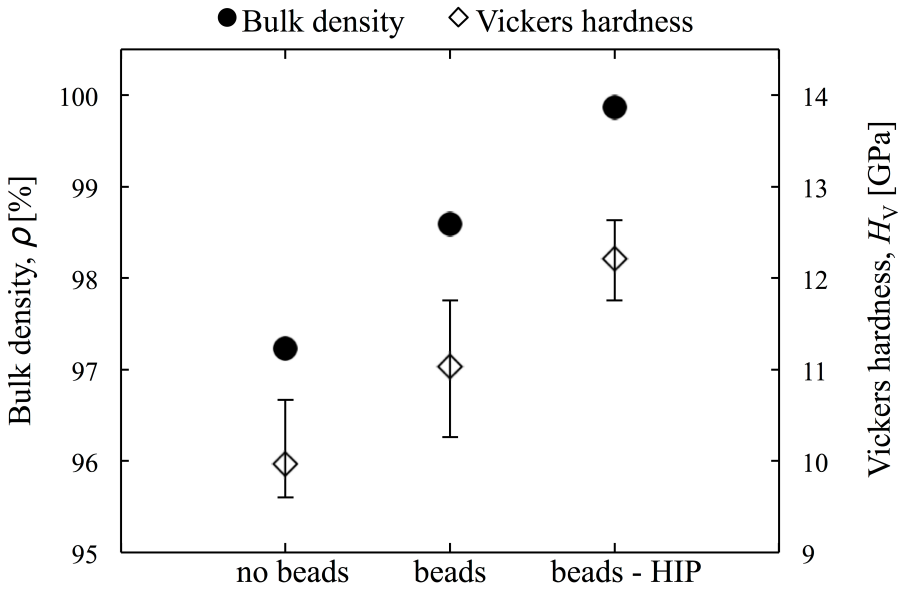

Fig. 2.7. Comparison of mechanical properties of $Y_2Ti_2O_7$ ceramics, before and after HIP

In summary, from the test results it can be confirmed that mechanical properties of the sintered ceramics are improved with the increasing of sintering pressure and with the minimizing of particle size of the $Y_2Ti_2O_7$ powder. Among all samples, the one sintered at 25 MPa from beads-milled powder shows the best mechanical properties, thus it was chosen for fabricating the sandwiches.

The analysis results have pointed out that higher the sintering pressure is applied, the denser the ceramics will be obtained. However, the highest pressure that was used to hot-press $Y_2Ti_2O_7$ ceramics is 25 MPa. It was confirmed that samples sintered at higher pressures (data not shown), are very easy to be broken. This is because in uniaxial pressure sintering,

when very high pressure is applied in one direction, some cracks might appear and develop inside the sample, and finally might break the sample. A proper technique to further densify the ceramics but avoid cracking them is using HIP. Because the pressure in HIP are uniformly applied to a sample in all directions, the sample will be very rarely broken. Furthermore, the isostatic pressure make the pores shrink, which in turn improve the density of the ceramic. As shown in Figure 2.7, after being processed with HIP, the density and hardness of $Y_2Ti_2O_7$ ceramic was improved to 99.87% and 12.21 GPa, respectively. These values are obviously higher than those of un-processed ceramic, as well as higher than those sintered by He *et al*.(51) (99.4%) and Wada *et al*.(60) (97.8%), and to the best knowledge of the author are also the highest values in $Y_2Ti_2O_7$ ceramics that have ever been sintered.

2.3.2. Ceramic-metal sandwiches and analysis results

These densified ceramics, as well as the ones hot-pressed from as-synthesized $Y_2Ti_2O_7$ powder, were used to fabricate the sandwich with aluminum to investigate their ability to resist to the penetration of molten metal. In the case of the sandwich S560, because the heating temperature was much lower than the melting point (660 °C), the aluminum foils were not molten and stuck to the discs (data not shown). When the heating temperature was increased to the melting point (the sandwich S660), the foils started to be molten and adhered to the discs' surfaces. However, it is very simple to separate the discs by hand from each other. It can be seen that there are some traces of molten Al remaining on the surface of the discs (see Fig. 2.8a), however, from the XRD pattern (see Fig. 2.8b), the surface is confirmed $Y_2Ti_2O_7$ single phase, which means there was no reaction between the surface and molten Al in this case.

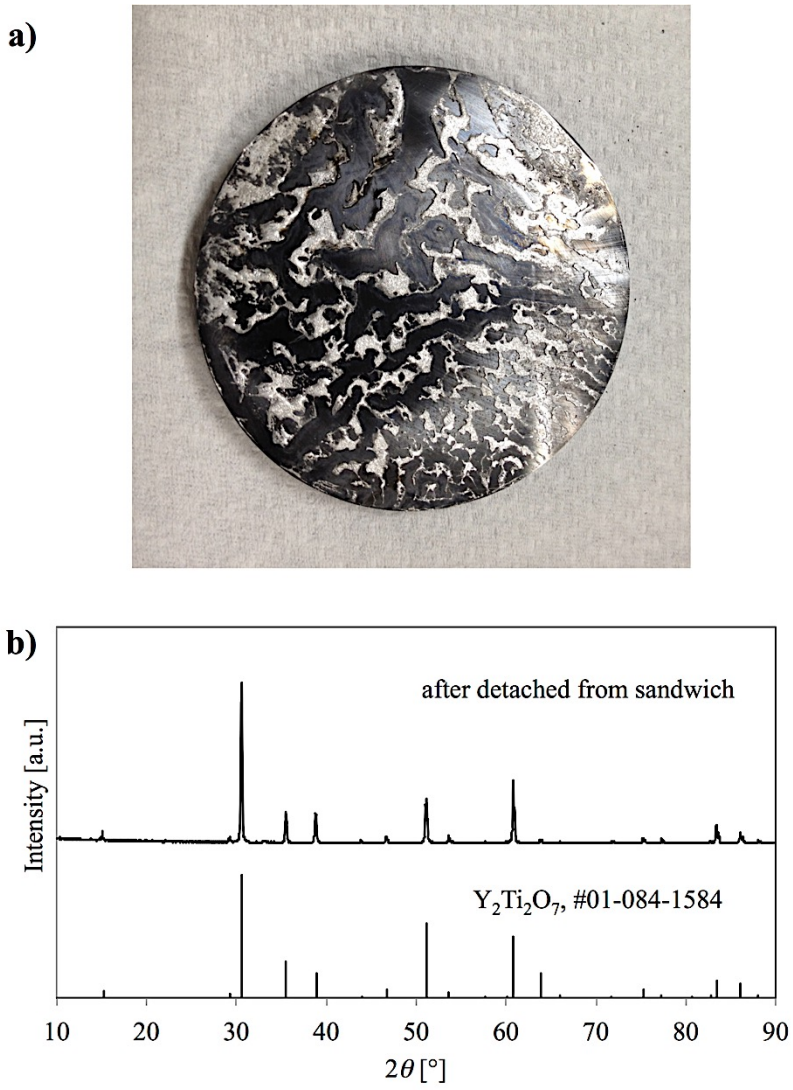

Fig. 2.8. S660 sandwich with: (a) optical photographs of $Y_2Ti_2O_7$ disc (after detached from the sandwich). Some traces of molten aluminum can be seen on the surface and (b) XRD pattern of the surface.

When the heating temperature was changed to 800 °C (higher than the melting point), the molten foils have stuck to the ceramic surface so strongly that the two discs cannot be separated. The cross-section of this sandwich was also subjected to XRD to investigate the reaction between the molten metal and the ceramic. As the Al layer is very thin, the intensity is plotted in Figure 2.9 in logarithmic scale to highlight the small peaks. The XRD pattern of

the interface between Al and $Y_2Ti_2O_7$ (Fig 2.9) reveals no other phases than those of Al and $Y_2Ti_2O_7$, indicating that there was no reaction between them during the heating process.

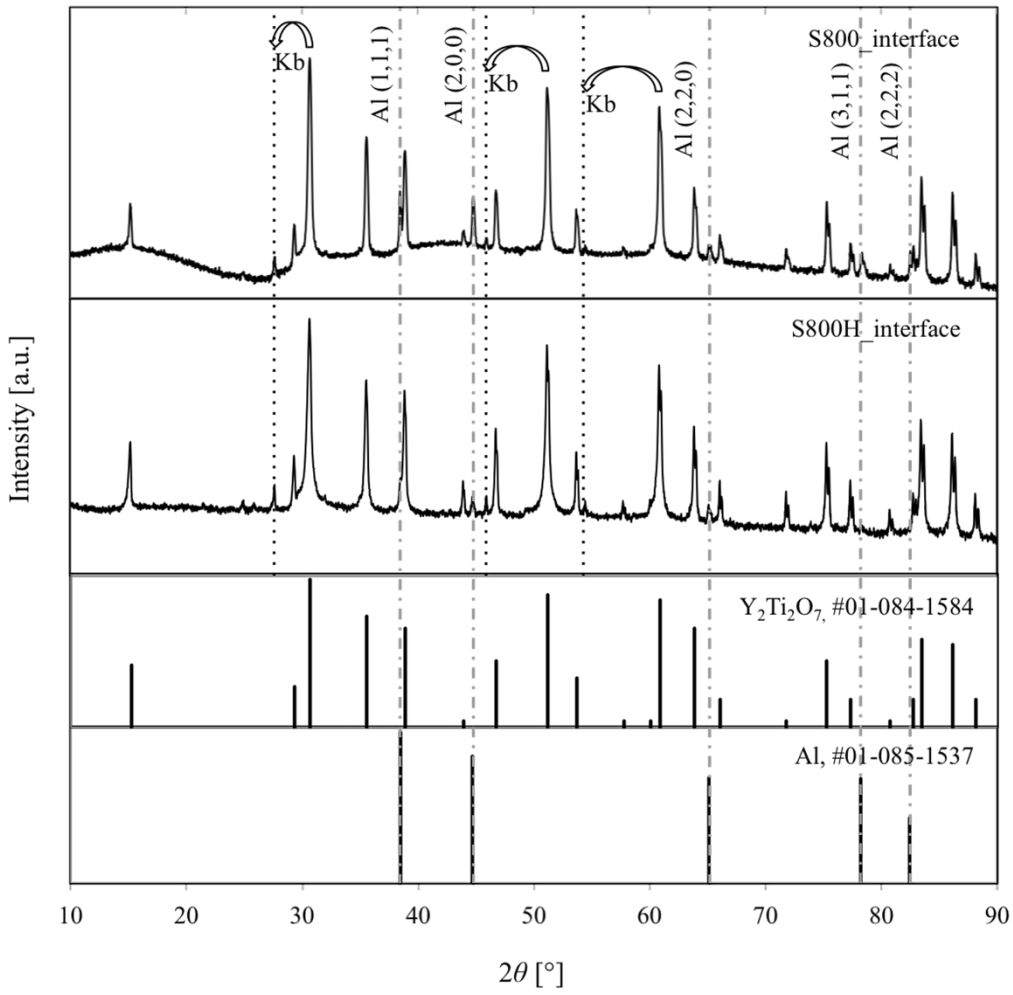

Fig. 2.9. XRD pattern (in log scale) of the interfaces of S800 and S800H sandwiches

Figure 2.10a and Figure 2.10c show SEM micrographs of the interfaces, revealing dark and 10 µm- thick layers located in the middle. Figure 2.10b displays the EDS result taken from position 1 in Figure 2.10a, confirming that the dark areas in these micrographs correspond to aluminum. While according to the EDS analysis of position 2 in Figure 2.10c, which is displayed in Figure 2.10d, the bright and white areas in these micrographs are indicated to be $Y_2Ti_2O_7$ (the molar ratio is Y : T : Al = 51 : 49 : 0, approximate to 1 : 1 : 0).

The EDS analyses (see Table 2.3) also reveal that there are small amount of $Y_2Ti_2O_7$ existing in Al layers, corresponding to slightly dark and gray areas (position 3 in the two micrographs). For instance, the molar ratio of the position 3 in Figure 2.10d is 1.07 : 0.8 : 98.13. It is considered that during the cutting process, small fragments of $Y_2Ti_2O_7$ were drafted to the Al domains and trapped there.

The EDS analyses were also performed on the two regions in the ceramics domains to study the penetration of molten Al into $Y_2Ti_2O_7$. Because of the difficulty in detecting the amount of oxygen by this technique, the atomic percent of oxygen is excluded from the compositional analysis. In both two sandwiches, region 1 extends from the interface to 10 μm depth in the ceramic, while region 2 extends from the end of region 1 to 30 μm depth in $Y_2Ti_2O_7$ (see Fig 2.10a and Fig 2.10c). In each region, at least 10 different spots were inspected and the atomic percent was calculated by average method. As shown in Table 2.3, the percentage of aluminum atoms in the region 1 (from the interface to 10 μm depth in the ceramic), in the two sandwiches S800 and S800H are 2.64 % and 0.61 %, respectively. In the region 2 (10 to 30 μm from interface), these numbers are 0.45% and 0.17%, correspondingly. These results reveal that there is a small amount of Al ions penetrated into the $Y_2Ti_2O_7$ structure. However, this penetration is very limited and decreasing with the increase of the distance to the interface. This reduction of molten Al penetration is even more obvious in the case of S800H sandwich.

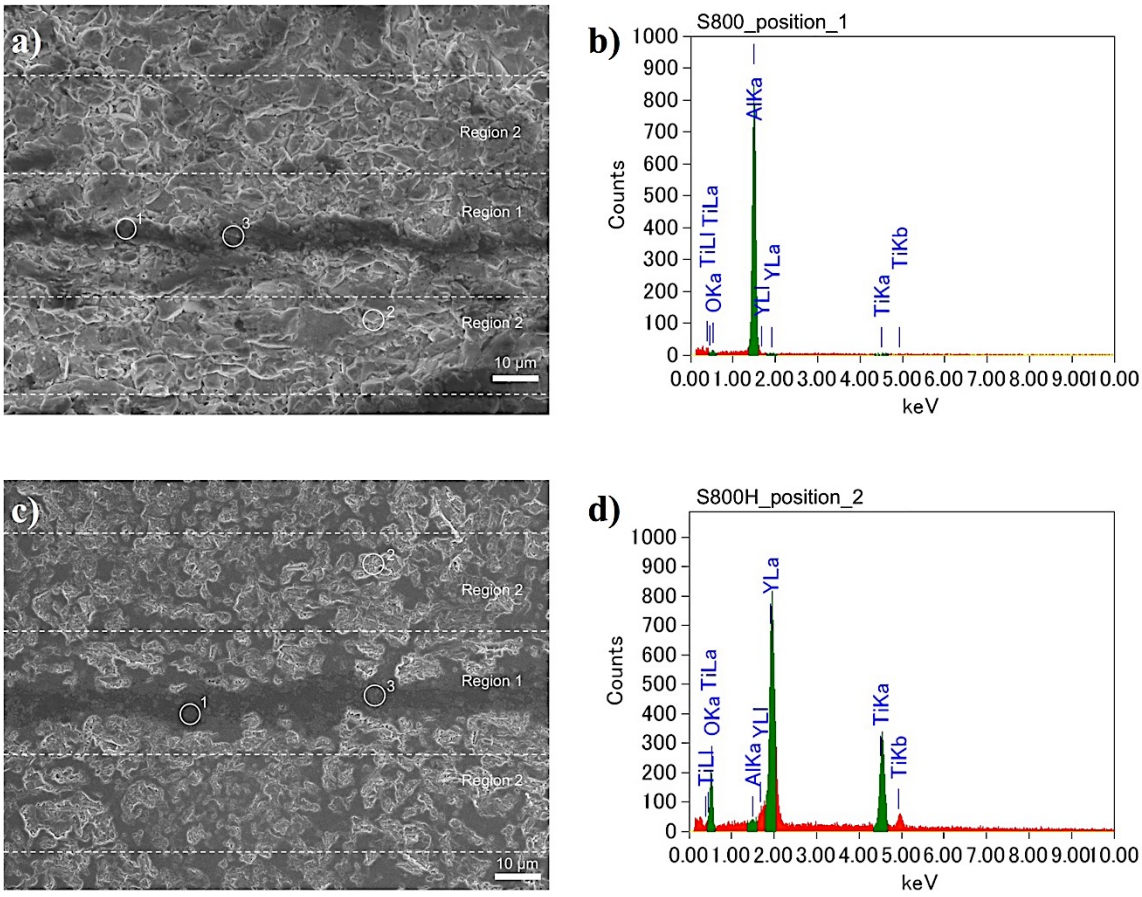

Fig. 2.10. Cross section microstructures of S800 and S800H sandwiches with: (a and b) SEM micrograph and EDS spectroscopy of S800 (position 1), (c and d) SEM micrograph and EDS spectroscopy of S800H (position 2)

From these results, it can be concluded that the penetration level of molten Al into $Y_2Ti_2O_7$ ceramics is negligible, especially in the case of the ceramic processed with HIP. It has been considered that the presence of pores on the grain boundaries and inside the grains of the ceramics caused the penetration of the metallic particles into the ceramics. The densification performed with HIP had decreased the quantity and size of pores inside the $Y_2Ti_2O_7$ ceramics, therefore enabled the ceramics reduce the penetration level of external molten Al particles.

Table 2.3. Summary of EDS composition analysis results at the interface regions

	Al (at%)	Y (at%)	Ti(at%)
S800			
Position 1	97.73	1.02	1.25
Position 2	0	51.7	48.2
Position 3	91.45	5.63	2.92
Region 1 (0 - 10μm)	2.64	58.89	38.47
Region 2 (10 - 30μm)	0.45	57.75	41.8
S800H			
Position 1	97.29	1.5	1.21
Position 2	0	51	49
Position 3	98.13	1.07	0.8
Region 1 (0 - 10μm)	0.61	53.8	45.59
Region 2 (10 - 30μm)	0.17	54.88	44.95

2.4. Conclusions

In this chapter, $Y_2Ti_2O_7$ ceramic discs, fabricated by hot-pressing method, were used to synthesize sandwich with aluminum foils by heat treatment at 800°C for 1 h. Following conclusions can be drawn from the obtained results:

(1) The mechanical properties of the $Y_2Ti_2O_7$ ceramics were improved by increasing the sintering pressure and minimizing the particle size of the powder.

(2) The HIP process is proven to be effective in increasing the density and improving the hardness of the sintered ceramics.

(3) There was no reaction between $Y_2Ti_2O_7$ and molten Al during the heating process. Because of the existence of the pores in $Y_2Ti_2O_7$ sintered bodies, molten Al has penetrated into the ceramics. However, it is confirmed from EDS analyses that this penetration is not

significant and can be reduced by the densification of the ceramics, which was done by HIP process.

Chapter 3: Low thermal conductivity $Y_2Ti_2O_7$ - a candidate for thermal/environmental barrier coatings

Abstract:

In this chapter, ceramic matrix composites of yttrium titanate ($Y_2Ti_2O_7$) with nickel (Ni) or silicon carbide (SiC) were synthesized to investigate their potential as candidate materials for thermal/environmental barrier coatings. The composites were sintered by hot-pressing at 25 MPa. The mechanical properties of the composites including bulk density, Vickers hardness, and fracture toughness were evaluated. The measurements indicated that the incorporation of Ni or SiC has a positive effect in terms of enhancing the fracture toughness of the composites. Microstructural observations revealed that $Y_2Ti_2O_7$/Ni is an inter/intra nanocomposite, while $Y_2Ti_2O_7$/SiC has characteristics of a network microstructure composite. In addition, X-ray diffraction and energy dispersive X-ray spectroscopy analyses confirmed $Y_2Ti_2O_7$ was chemically stable against Ni, but reacted with SiC to form silicates during the sintering process. The mechanisms for these reactions are also proposed.

3.1. Introduction

To be a good candidate material for T/EBC, the material should be chemically stable at high temperatures when it interacts with other layers, and mechanically strong to protect the substrate from physical damage. While there are various materials and structures for the intermediate layers (20,23,70), the substrate layer is fundamentally Ni-based alloy or SiC_f/SiC_m. To give an extensive evaluation of the feasibility of $Y_2Ti_2O_7$ as a T/EBC, it is essential to investigate the interaction between this material and Ni (or SiC) at high temperature. This chapter proposes a method for such an evaluation by the fabrication and characterization of composites consisting of a $Y_2Ti_2O_7$ matrix and Ni (or SiC) fillers.

SiC-incorporated nanocomposites were first successfully developed 25 years ago with significant improvements in both strength and toughness (32). Since then, numerous studies have been conducted on the fabrication and characterization of many types of ceramic-based nanocomposites with both ceramic and metallic fillers (33–36). However, there have been many intensive studies regarding the synthesis and characterization of $Y_2Ti_2O_7$/Ni or $Y_2Ti_2O_7$/SiC composites, and no research on the interaction between $Y_2Ti_2O_7$ and gas-turbine-blade materials at high temperatures.

Therefore, in this chapter, $Y_2Ti_2O_7$/Ni and $Y_2Ti_2O_7$/SiC CMCs (filler volume content ranging from 5 to 20 vol%) were synthesized by solid state reaction and hot-pressing. The mechanical properties of the composites, including bulk density, Vickers hardness, and fracture toughness, were evaluated. In addition, the microstructure and phase of the composites were analyzed to investigate the reaction between the $Y_2Ti_2O_7$ matrix and the fillers during the sintering process. The purpose of this chapter is to evaluate the applicability of pyrochlore $Y_2Ti_2O_7$ as a candidate material for T/EBC in gas turbine engine.

3.2. Experimental Procedure

3.2.1. Fabrication of $Y_2Ti_2O_7$/Ni and $Y_2Ti_2O_7$/SiC nanocomposites

$Y_2Ti_2O_7$ powder was prepared by the same method described in previous chapter. To synthesize $Y_2Ti_2O_7$/Ni composites, a solution chemistry method was employed because it was confirmed to provide a fine dispersion of metal particles in the ceramic matrix (33,71). First, nickel nitrate $Ni(NO_3)_2 \cdot 6H_2O$ (98%, Wako Pure Chemicals) was mixed with $Y_2Ti_2O_7$ powder and ball-milled in high purity ethanol (99.5%) for 24 h. After solvent evaporation and drying overnight at 80 °C, the powder mixture was ground with a mortar and pestle before being calcined in air at 400 °C for 2 h to obtain nickel oxide (NiO) from the thermal decomposition of $Ni(NO_3)_2 \cdot 6H_2O$. The $Y_2Ti_2O_7$/NiO mixture powder was then placed in an

alumina boat and heated in a tube furnace under a 100 mL min^{-1} flow of a 97% Ar + 3% H_2 gas mixture at 800 °C for 2 h, which resulted in the complete reduction of NiO into nickel (Ni). The $Y_2Ti_2O_7$/Ni powder mixture was then dry ball-milled for 24 h to obtain a homogeneous state.

$Y_2Ti_2O_7$/SiC powder mixtures were prepared by mixing $Y_2Ti_2O_7$ with β-SiC nanopowder (Sigma Aldrich) and ball-milling in 99.5% ethanol for 24 h. The mixture was dried at 80 °C overnight, dry ball-milled for 12 h, and then sieved through a 100 mesh screen.

Finally, the as-prepared powder mixtures of $Y_2Ti_2O_7$/Ni or $Y_2Ti_2O_7$/SiC were hot-pressed in a gas-pressure-sintering furnace (Fuji Dempa Kogyo, FVPHP-R-5, FRET-18) to obtain sintered discs (20 mm diameter). The $Y_2Ti_2O_7$/Ni composites were sintered in an Ar atmosphere at 25 MPa and 1340 °C for 4 h. The $Y_2Ti_2O_7$/SiC composites were sintered under the same conditions of atmosphere and pressure, but at a higher sintering temperature of 1500 °C for 1 h. The sintering temperatures were selected as 1500 °C, and 1340 °C, based on the common target for the surface temperature of SiC_f/SiC_m turbine blades (23,72), and the maximum surface temperature for the current Ni-based superalloy turbine blades (23,73), respectively. The soaking time was increased to 4 h, to ensure a dense $Y_2Ti_2O_7$ matrix can be obtained at the low sintering temperature of 1340 °C. Two monolithic $Y_2Ti_2O_7$ ceramics were also sintered (one at 1340 °C for 4 h and another at 1500 °C for 1 h, both in an Ar atmosphere at 25 MPa) for comparison. In both sintering processes, the heating rate was 10 °C min^{-1}. The $Y_2Ti_2O_7$/Ni sintered composites with 0, 5, 10, 15, and 20 vol% Ni fillers are denoted as YN_x (x = 0, 5, 10, 15, and 20, respectively). Similarly, the $Y_2Ti_2O_7$/SiC composites with 0, 5, 10, and 20 vol% SiC are denoted as YS_y (y = 0, 5, 10, and 20, respectively). Table 3.1 summarizes all of the sintered composites and their bulk densities, which were measured by the Archimedes method in high purity toluene.

Table 3.1. Bulk density of $Y_2Ti_2O_7$/Ni and $Y_2Ti_2O_7$/SiC sintered composites

	$Y_2Ti_2O_7$/Ni composites					$Y_2Ti_2O_7$/SiC composites			
Filler content (vol%)	0	5	10	15	20	0	5	10	20
Designation	YN_0	YN_5	YN_{10}	YN_{15}	YN_{20}	YS_0	YS_5	YS_{10}	YS_{20}
Bulk density (%)	99.5	99.3	97.8	96.4	93.3	99.6	98.9	96.9	92.8

3.2.2. Analysis and characterization

The thermal diffusivity and specific heat capacity of the sintered $Y_2Ti_2O_7$ ceramic were measured according to the ASTM E-1461 standard, using a laser flash system for thermophysical properties (Netzsch, LFA 457 Microflash). 10 mm diameter and 1 mm thick pellets were cut for measurements from the sintered discs. The measurements were conducted from room temperature to 700 °C in 100 °C intervals under flowing Ar gas (120 mL min^{-1}).

The morphology and particle size of the powder mixture were observed using transmission electron microscopy (TEM; JEM-2000FX, Jeol Ltd.). Phase identification of the powder mixtures and sintered nanocomposites was conducted using X-ray diffraction (XRD; RINT 2500PC, Rigaku, Japan).

Mechanical properties, including Vickers hardness H_V, and fracture toughness K_{IC}, were investigated. H_V was measured according to the same standard described in previous chapter. K_{IC} was calculated according to the indentation method using the Niihara equation (3.1) (74):

$$K_{IC} = 0.203 H_V a^2 c^{-3/2}, \quad (3.1)$$

where a and c are the half diagonal length of the Vickers indentation and the half length of the crack, respectively.

The microstructures of the sintered composites and Vickers crack indentations were observed using scanning electron microscopy (SEM; Hitachi High-Technologies, TM-3000). The composition of the composites was analyzed using field-emission scanning electron microscopy (FE-SEM; JSM-6700F, Jeol Ltd.) with energy-dispersive X-ray spectroscopy (EDS; JED-2201F, Jeol Ltd.). For observation, samples were coated with a 5 nm osmium layer using a hollow cathode plasma chemical vapor deposition (CVD) coater (HPC-1SW, Vacuum Device Inc.).

3.3. Results and Discussion

3.3.1. Thermal properties of $Y_2Ti_2O_7$

The thermal conductivity is calculated using the measured thermal diffusivity, density, and specific heat capacity according to the equation (3.2):

$$k = \alpha \times \rho \times Cp, \tag{3.2}$$

where k, α, ρ, and Cp are the thermal conductivity, thermal diffusivity, bulk density, and specific heat capacity, respectively. The thermal diffusivity, specific heat capacity, and thermal conductivity of the $Y_2Ti_2O_7$ pyrochlore are shown in Figure 3.1. For comparison, the thermal conductivity of 7 mol% YSZ (7YSZ) from Ref. (15) is also plotted. The pyrochlore has a thermal conductivity in the range of 2.25–2.6 W m^{-1} K^{-1}. At each of the investigated temperatures up to 500 °C, the thermal conductivity of $Y_2Ti_2O_7$ was 0.03–0.04 W m^{-1} K^{-1} lower than the corresponding value for 7YSZ. Above 500 °C, the thermal conductivity increased slightly and was only slightly higher than that for 7YSZ at 700 °C. Thus, the thermal conductivity of $Y_2Ti_2O_7$ is generally more stable and lower than that of 7YSZ, as predicted.

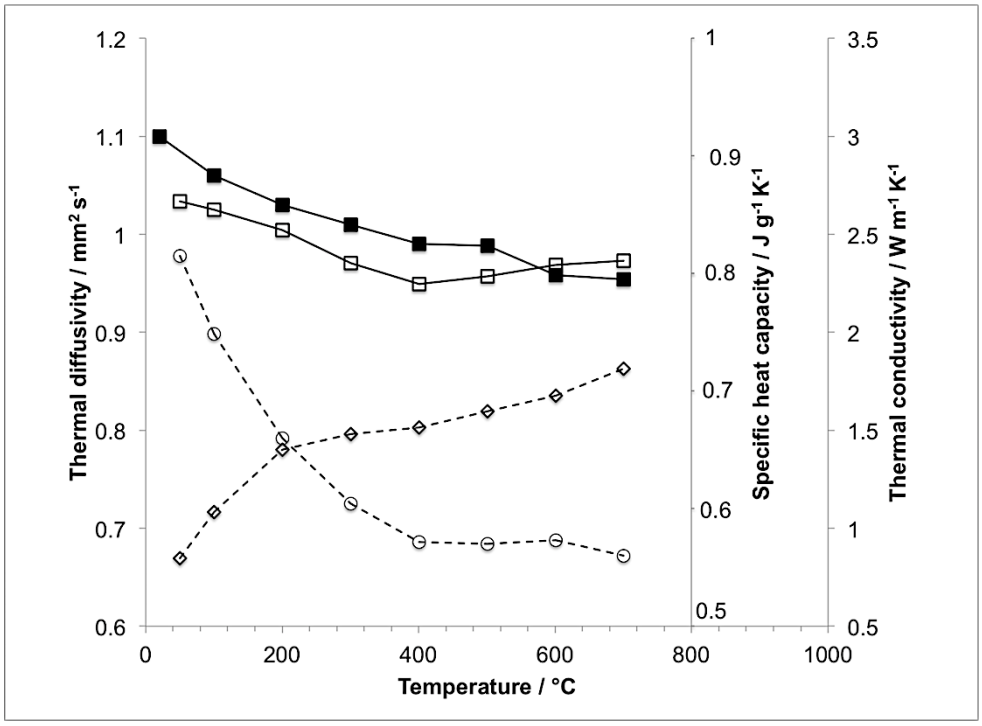

Fig. 3.1. Thermal diffusivity (○), specific heat capacity (◇), and thermal conductivity (□) of $Y_2Ti_2O_7$ sintered pellet as a function of temperature. Thermal conductivity of 7YSZ sintered pellet (■) is also replotted from Ref. (15) for comparison.

3.3.2. Synthesis and characterization of $Y_2Ti_2O_7$/Ni composites

The solution route has been previously (33,71) used to fabricate Al_2O_3/Ni composites. In those studies, after ball-milling and calcination, the nitrate was converted into NiO and coated on the Al_2O_3 particle surfaces. The nickel (II) oxide then reduced to Ni after heat treatment in hydrogen. As a result, the powder mixture was homogeneous with Al_2O_3 particles surrounded by Ni particles. Therefore, in the present work, it was expected that after a similar process, $Y_2Ti_2O_7$ would be surrounded by Ni particles, and this was confirmed, as shown in Figure 3.2a. The bright-field TEM image of the $Y_2Ti_2O_7$/15 vol% Ni powder mixture (Fig. 3.2b) shows quasi-spherical particles with sizes in the range of 50-500 nm, where the larger and darker particles surrounded by smaller and brighter particles. In this micrograph and the magnified micrograph (Fig. 3.2c), darker domains correspond to $Y_2Ti_2O_7$

particles because their heavier atoms (higher atomic number) interact and scatter electrons more strongly than Ni atoms. The dark (1) and bright (2) domains were confirmed to be $Y_2Ti_2O_7$ and Ni crystallites by selected area electron diffraction (SAED) analysis (Figs. 3.2d and 3.2e). The spotty pattern in Figure 3.2d and the ring pattern in Figure 3.2e indicate that $Y_2Ti_2O_7$ particles contain several larger crystallites, while Ni particles contain many smaller crystallites. The different contrast in the TEM micrograph of the Ni particle (Fig. 3.2c) indicates that it is a polycrystalline particle. The average size τ of Ni crystallites was calculated according to the Scherrer equation (3.3):

$$\tau = k\lambda/\beta\cos\theta, \qquad (3.3)$$

where k, the shape factor of the particle, is taken as 0.94 for quasi-spherical particles of cubic structure (75), λ is the X-ray wavelength (1.54186 Å), β is the full width at half maximum intensity (FWHM), and θ is the diffraction angle. The mean size of Ni crystallites calculated from the XRD pattern of the $Y_2Ti_2O_7$/15 vol% Ni powder mixture (Fig. 3, line a) was 44.1 nm. To avoid the uncertainty in β that may affect the accuracy of the calculation, the Halder-Wagner method (76) was also used to analyze the crystallite size. In this method, the major peaks of the large crystallite phase (i.e., $Y_2Ti_2O_7$ in this case) are used as a standard to correct the peak width of the test phase (i.e., Ni) and obtain more precise results (77). The Ni crystallite size calculated by the Halder-Wagner method was 44.7 nm, which is in agreement with that obtained from the Scherrer equation.

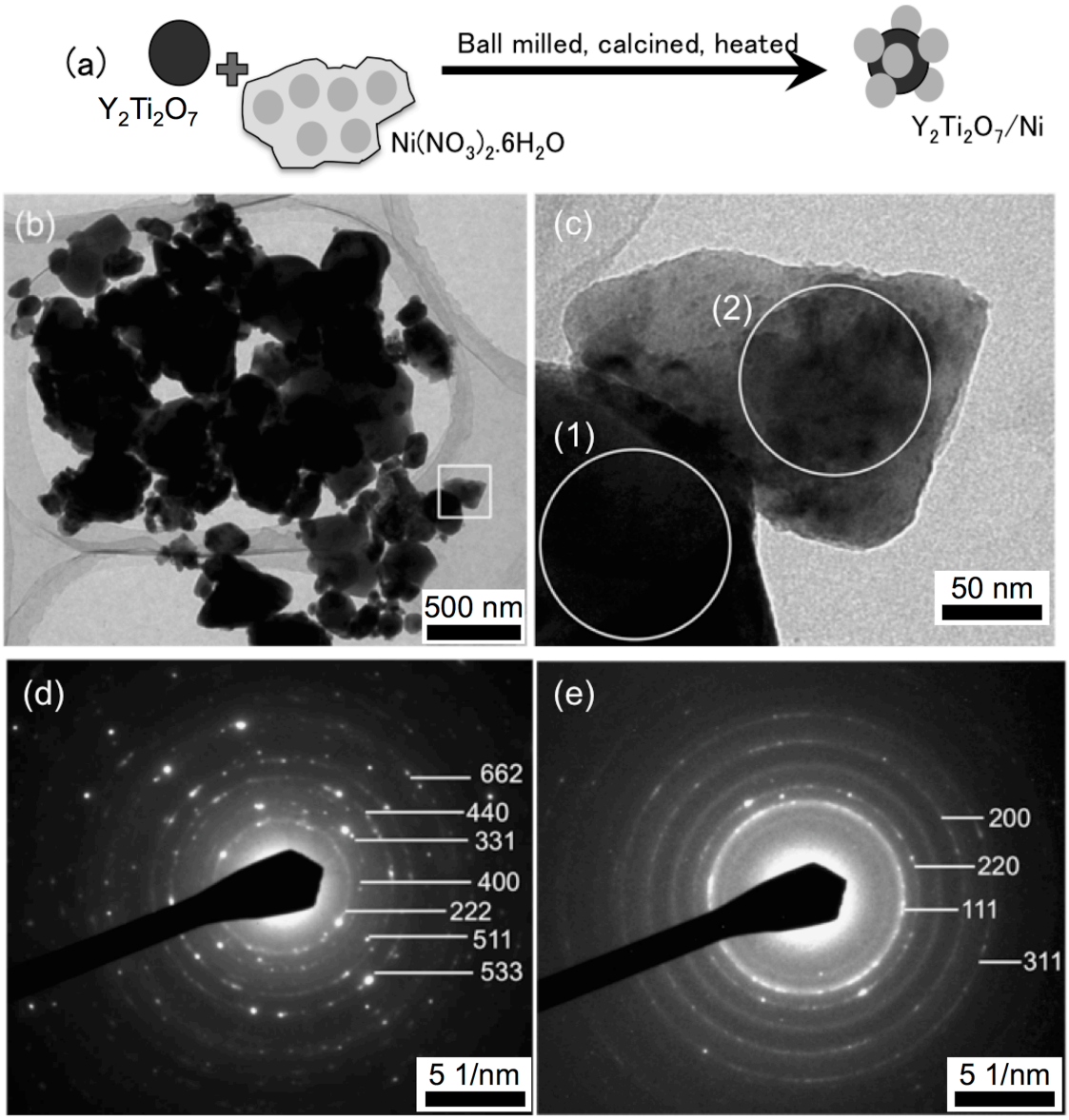

Fig. 3.2. Morphology of $Y_2Ti_2O_7$/Ni agglomerates: (a) Schematic illustration of agglomeration; (b) TEM micrograph showing $Y_2Ti_2O_7$/Ni agglomerate; (c) Magnified image of the square region marked in (b) showing a Ni particle attached on a $Y_2Ti_2O_7$ particle; (d and e) SAED patterns of regions (1) and (2) indicated in (c)

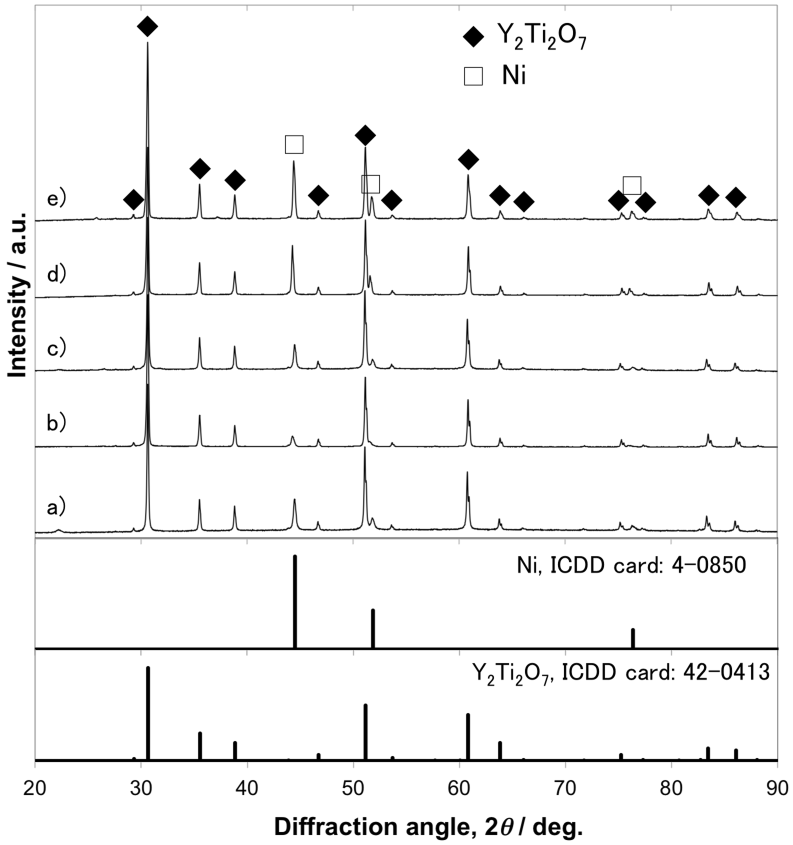

Fig. 3.3. XRD profiles for the starting mixture and sintered composites: $Y_2Ti_2O_7$/15 vol% Ni powder mixture (line a), YN_5 sintered composite (line b), YN_{10} sintered composite (line c), YN_{15} sintered composite (line d), YN_{20} sintered composite (line e).

Figure 3.3 also presents the XRD profiles for the sintered composites with different Ni content (5 to 20 vol%). All composites (lines b-e) have peaks at the same diffraction angles as the powder mixture (line a). The composites are thus identified to consist of $Y_2Ti_2O_7$ and Ni phases according to the ICDD cards. The absence of other peaks indicates that no chemical reaction between $Y_2Ti_2O_7$ and Ni occurred during the sintering process. The intensity of the Ni peaks increased with the addition of the fillers content and there was no peak shifting. On the other hand, there was no significant change in the peak sharpness of YN_{15} before and after sintering, which implies that there was negligible grain growth in the sintered composite.

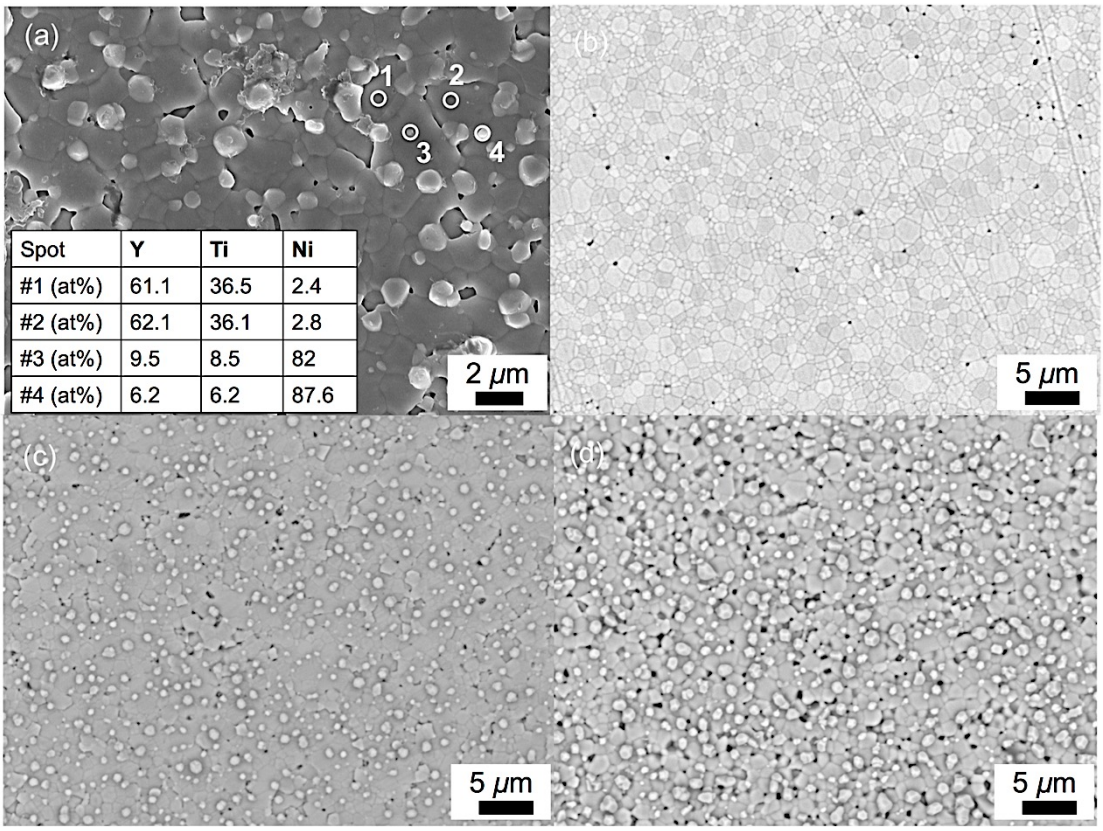

Fig. 3.4. (a) FE-SEM micrograph and EDS analysis results for the surface of the $Y_2Ti_2O_7$/15 vol% Ni sintered nanocomposite. Some Ni particles were broken during the grinding and polishing processes. SEM micrographs showing the microstructures of (b) YN_0, (c) YN_{10}, and (d) YN_{20}.

Fig. 3.4a shows the microstructure of the YN_{15} sintered composites. EDS analysis confirmed that the darker and larger structures are $Y_2Ti_2O_7$ grains (spots 1 and 2), while the brighter and smaller structures are Ni particles (spots 3 and 4). The grain size of $Y_2Ti_2O_7$ ranged from 0.3 to 3 μm, which is slightly larger than the $Y_2Ti_2O_7$ particle size observed using TEM. Ni particles were dispersed homogeneously and located not only at the grain boundaries but also inside $Y_2Ti_2O_7$ grains, which indicates that this is an intra/inter type nanocomposite (32). The microstructure of YN_0, YN_{10}, and YN_{20} shown in Fig. 3.4b-d, respectively, confirmed that the dispersion of Ni nanoparticles not only helps to restrain the growth of $Y_2Ti_2O_7$ grains but is also beneficial to produce a more homogeneous size

distribution. However, the disadvantage of this incorporation is that at high concentrations, filler particles agglomerate and grow into larger particles (see Fig. 3.4d), which can inhibit densification of the composite. As a result, the relative density of the composite decreases with increasing filler content (see Table 3.1).

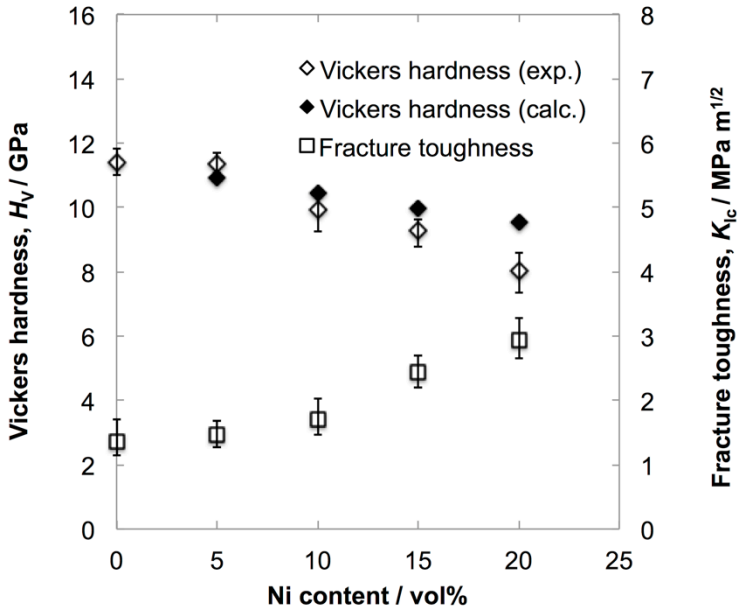

Fig. 3.5. Experimental Vickers hardness (◇) and fracture toughness (□) of sintered $Y_2Ti_2O_7$/Ni composites as a function of filler content. Simulated Vickers hardness (◆) is also plotted for comparison.

Fig 3.5 shows that the room temperature Vickers hardness of the composites decreased gradually with an increase in the Ni content (11.41 for YN_0 versus 8.03 GPa for YN_{20}). Therefore, the incorporation of Ni particles is believed to have softened the composites. In addition, the increasing porosity in high Ni content composites may contribute to this degradation of hardness. The experimental hardness values were also compared with simulated values, calculated according to the rule of mixture. The hardness of pure Ni is taken as 1.96 GPa, converted from data measured by Jung et al. (78). All of the composites, except for the low Ni content YN_5, have experimental hardness values lower than the

corresponding calculated values because the calculation by rule of mixture did not take into account the decrease in density.

The homogeneous dispersion of Ni nanoparticles also affected the fracture toughness of the composites. The toughening effect of Ni dispersions on composites has been reported previously (33,79). In the present research, improvement in the toughness was very slight at low Ni content (5 and 10 vol%), but more impressive at higher Ni concentrations (15 and 20 vol%), with a 2.2-fold enhancement from 1.35 MPa $m^{1/2}$ for YN_0 to 2.94 MPa $m^{1/2}$ for YN_{20}. The toughening mechanism is generally related to role of ductile particles in bridging and deflecting cracks (80). The former is more common in network microstructure composites, while the latter is essential in particle dispersion composites (33,79). Crack propagation in the present composites at high Ni concentration is principally hampered by deflection, as shown in Fig. 36e-f. In addition, Sekino et al. (33) also pointed out that small dispersed particles have minimal effect on toughness improvement, i.e., cracks propagate through small particles more easily than larger particles. In the case of YN_5 (Fig. 3.6b), the Ni particles are too small, so that they have no significant effect on crack deflection. For YN_{20}, ductile particles with sizes of ca. 1 μm (Fig. 3.6c) hindered and deflected the propagation of indentation cracks, and thereby contributed to the improved toughness.

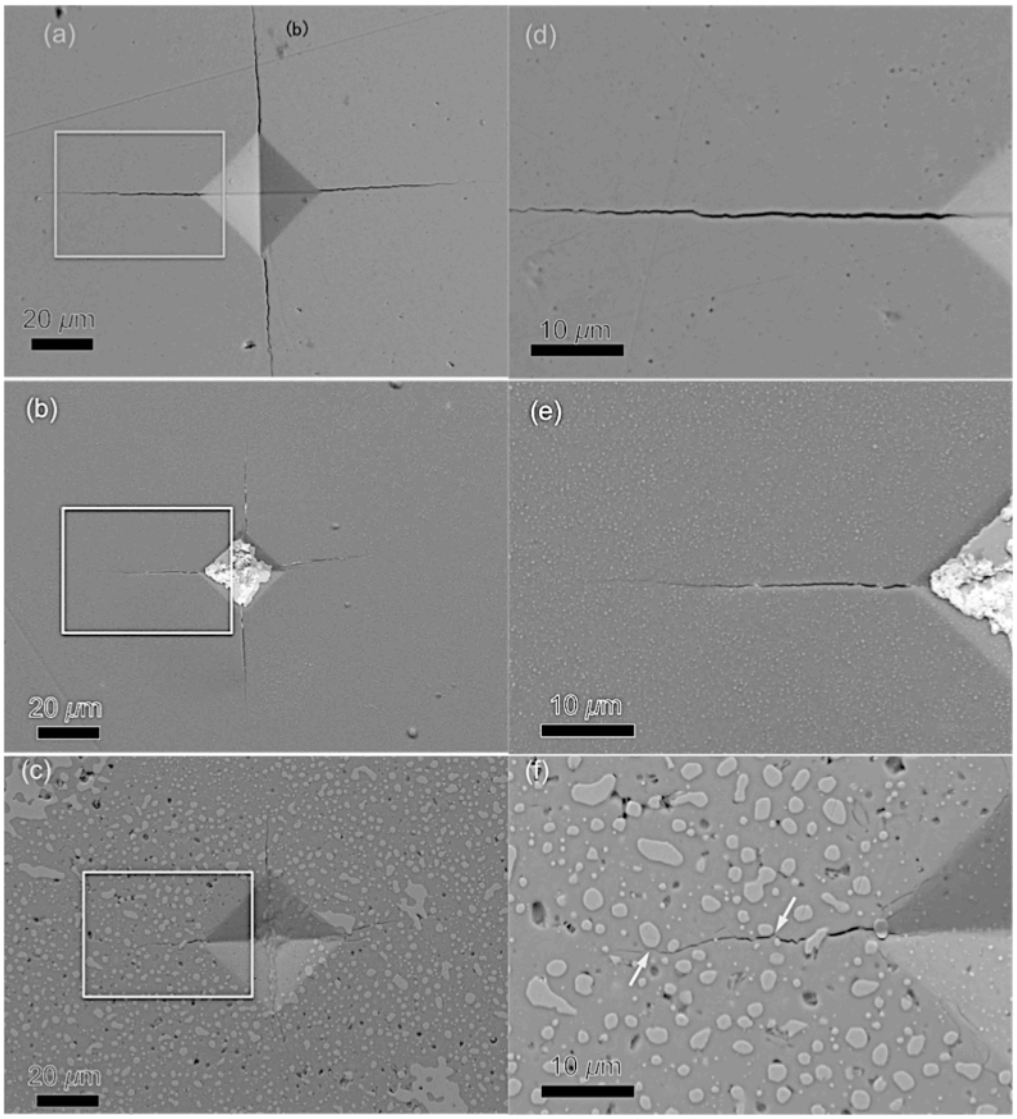

Fig. 3.6. SEM micrographs of Vickers indentations on (a) YN_0, (b) YN_{15}, and (c) YN_{20} composites surfaces; (d–f) Magnified images of the square regions marked in (a-c), respectively. The white arrows in (f) indicate crack deflection.

3.3.3. Synthesis and characterization of $Y_2Ti_2O_7$/SiC composites

Figure 3.7a shows the microstructure of YS_{10} composite observed with FE-SEM using the secondary electron imaging (SEI) method. According to the contrast, three different types of domain are evident in the micrograph: bunches of small grains (area I), large grains with many tiny dots (area II), and lumpy particles (area III). Figure 3.7b shows a higher

magnification SEM image with bunches of small grains with blurred boundaries, and a lumpy particle. The tiny dots in the grains appear to be fragments drifted from lumpy particles during polishing. Figure 3.7c shows a backscattered electrons (BSE) image taken from the same region in Figure 3.7a, with a better contrast so that different domains can be easily distinguished. EDS analysis was conducted on this sample (spots 1 to 8 in Fig. 7c) to determine the elemental composition in each area. Although it is difficult to accurately detect the amount of oxygen by this technique, the atomic percent of oxygen is also included to give an initial evaluation for the composition of different domains. Carbon is excluded from the analysis to avoid inaccurate results caused by carbon atoms from the graphite sheet during sintering rather than from SiC. Area I has all species present: Y, Ti, O, and Si (spots 1, 8), which suggests that this could be a domain of the $Y_2Ti_2O_7$ and SiC mixture, or their reaction products if reaction occurred. Area II is considered to be equivalent to pure $Y_2Ti_2O_7$ grains (spots 3, 6, 9), without the presence of any Si atoms. In Area III, the dominant presence of Ti and O, and the absence of Si (spots 2, 5, 7) suggest that this domain could be an oxide of titanium. Therefore, it is considered that reactions did occur between $Y_2Ti_2O_7$ and SiC during the sintering process, and their products could be titanium oxides and one or several silicates.

Figure 3.8a shows XRD profiles for the powder mixtures (lines a-c) and sintered composites (lines d-f). Only the two phases of $Y_2Ti_2O_7$ and SiC were confirmed in the diffraction patterns of the powder mixtures, in which most of the SiC peaks were overlapped by $Y_2Ti_2O_7$ peaks, except for the (220) peak at $2\theta = 60.38°$. The patterns for the sintered composites show more evidence of reactions in the presence of other phases, which were identified to be Y_2SiO_5, β-$Y_2Si_2O_7$ (keiviite-(Y)), and rutile TiO_2. From EDS analysis and this XRD result, it can be inferred that the lumpy particles in Figure 3.7a are rutile TiO_2, and

the bunches of small grains are the domains of a mixture of $Y_2Ti_2O_7$, SiC, Y_2SiO_5, and $Y_2Si_2O_7$.

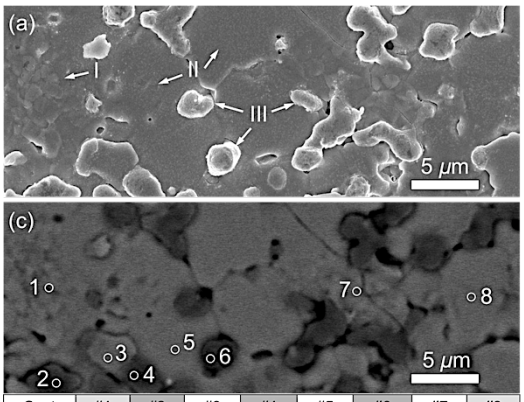

Spot	#1	#2	#3	#4	#5	#6	#7	#8
O (at%)	63.3	65.74	62.94	60.13	61.31	61.04	59.66	64.12
Si (at%)	5.43	-	0.24	-	0.27	-	4.68	0.22
Ti (at%)	12.44	32.82	19.49	38.45	18.83	33.51	15.35	17.55
Y (at%)	18.84	1.44	17.33	1.42	19.58	5.44	20.31	18.12

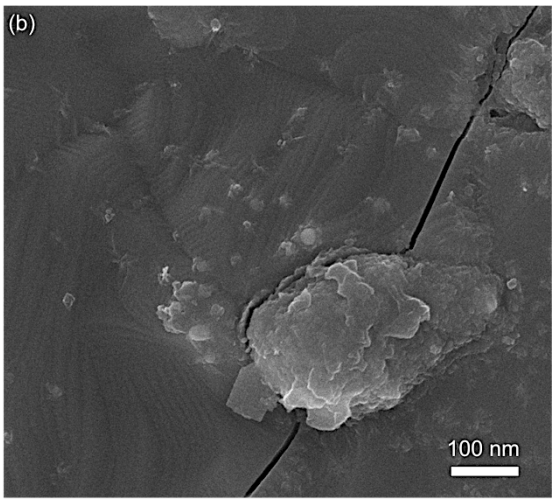

Fig. 3.7. (a) Low and (b) high magnification FE-SEM micrographs (SEI images) of $Y_2Ti_2O_7$/10 vol% SiC sintered nanocomposite. (c) BSE image of the same region in (a). The inset of (c) shows EDS results for spots 1–8 indicated in the BSE image.

Here, the author proposes a reaction mechanism to explain the appearance of Y_2SiO_5, $Y_2Si_2O_7$, and TiO_2. Tamura et al. (34) reported that after 2 h of heat treatment at 750 °C in an open SiO_2 container, synthesized $Y_2Ti_2O_7$ was partly decomposed into TiO_2 (both anatase and rutile) and Y_2O_3. After that, these two phases could reform to produce $Y_2Ti_2O_7$ by annealing at higher temperatures. In the present work, it is possible that during the process of heating the powder mixture to sintering temperature, $Y_2Ti_2O_7$ could be partly decomposed to Y_2O_3, anatase and rutile TiO_2, according to the following reaction:

$$Y_2Ti_2O_7 \rightarrow Y_2O_3 + 2TiO_2 \qquad (I)$$

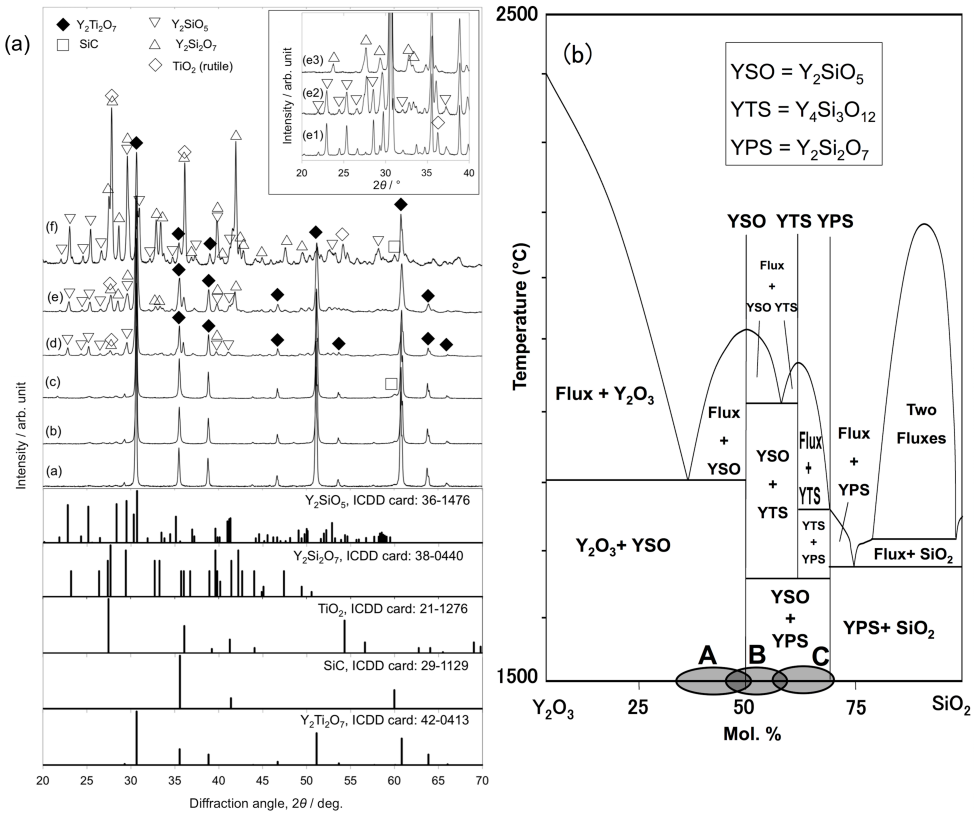

Fig. 3.8. (a) XRD profiles for 5, 10, 20 vol% SiC powder mixtures (lines a–c) and the corresponding sintered composites: YS_5, YS_{10}, YS_{20} (lines d–f). The inset shows XRD patterns (2θ range from 20° to 40°) for $Y_2Ti_2O_7$/10 vol% SiC composites sintered at 1400 (line e1), 1500 (line e2), and 1700 °C (line e3). (b) Y_2O_3-SiO_2 phase diagram reproduced from Ref. (38), with marked zones A, B, C where reactions occurred.

Most of the anatase would then be transformed to rutile at around 1000 °C (81). The decomposed Y_2O_3 readily reacts with SiO_2, which is typically present at the surface of SiC powder particles (82), to form yttrium silicates. The main products would be yttrium monosilicate (Y_2SiO_5) or yttrium disilicate ($Y_2Si_2O_7$), depending on the molar ratio of Y_2O_3 and SiO_2 available (83), as follows:

$$Y_2O_3 + SiO_2 \rightarrow Y_2SiO_5 \qquad \text{(II)}$$

$$Y_2O_3 + 2SiO_2 \rightarrow Y_2Si_2O_7 \qquad \text{(III)}$$

There are no peaks of the individual Y_2O_3 phase in the XRD patterns of the composites (lines d, e, f); therefore, it can be deduced that if some Y_2O_3 still remained after reactions (II) and (III), then it would react with rutile TiO_2 to form $Y_2Ti_2O_7$ at the sintering temperature:

$$Y_2O_3 + 2TiO_2 \rightarrow Y_2Ti_2O_7 \qquad \text{(IV)}$$

It is also noted that the intensity of the $Y_2Ti_2O_7$ peak decreased considerably when the SiC content was changed from 5 to 10, and 20 vol%, concurrently with the increase in the intensities of the silicate peaks. Y_2SiO_5 peaks and a few negligible $Y_2Si_2O_7$ peaks also appear in the pattern of the YS_5 composite, which indicate the dominance of Y_2O_3 to SiO_2 in the mixture. Thus, reaction (II) is considered to be the main reaction (zone A on the phase diagram in Fig. 3.8b). When the SiO_2:Y_2O_3 molar ratio increases as in YS_{10}, then the appearance of many $Y_2Si_2O_7$ peaks that are stronger in intensity implies that reaction (III) occurs somewhere in zone B. The area of reactions moved to zone C in the case of the YS_{20} composite, of which the pattern shows $Y_2Si_2O_7$ as the dominant phase. To investigate the effect of temperature on these reactions, two other samples of $Y_2Ti_2O_7$/10 vol% SiC composites were also sintered at 1400 and 1700 °C, with all other sintering conditions the same. The XRD patterns of these composites are shown in the inset of Fig. 3.8a. Y_2SiO_5 peaks appeared in the composite sintered at 1400 °C, which indicates that reaction (II) occurred at this low temperature. For the composite sintered at 1500 °C, the Y_2SiO_5 peaks were weaker and $Y_2Si_2O_7$ peaks began to appear. The composite sintered at 1700 °C shows very weak Y_2SiO_5 peaks, while the $Y_2Si_2O_7$ peaks are stronger than the corresponding peaks for the composite sintered at 1500 °C. From these results, it can be concluded that reaction (II) occurred earlier at temperatures as low as 1400 °C, while reaction (III) only occurred at temperatures higher than 1400 °C and tended to become the dominant reaction when the temperature was higher than 1500 °C.

Because Y_2O_3 had participated in reactions (II) and (III), decomposed TiO_2 still remains as a segregated phase after the sintering process is completed, regardless of reaction (IV) occurring. According to the SiO_2-TiO_2 phase diagram (84), these two phases can coexist without reaction at temperatures below 1550 °C. At higher temperatures, SiO_2 melt or TiO_2 melt would be formed depending on the SiO_2:TiO_2 molar ratio. The amount of SiO_2 available was limited; therefore, at that time TiO_2 would be the dominant phase, which would result in the formation of a SiO_2 viscous melt. After the sintering process, the SiO_2 suspension was extruded and spilled out of the die. It is considered that a two-step sintering may help to avoid that unwanted extrusion as well as the reaction between $Y_2Ti_2O_7$ and SiO_2, e.g., a lower temperature step to recombine decomposed oxides into $Y_2Ti_2O_7$ and a higher temperature step to sinter $Y_2Ti_2O_7$ and SiC. However, this exceeds the scope of this thesis and will instead be considered in future research.

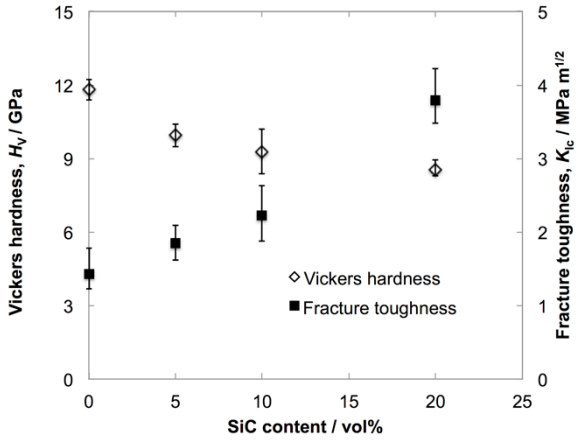

Fig. 3.9. Vickers hardness (◇) and fracture toughness (■) of $Y_2Ti_2O_7$/SiC sintered composites as a function of filler content.

Figure 3.9 shows the experimental Vickers hardness and fracture toughness of sintered composites as a function of the SiC content. Although the hardness was expected to improve after reinforcement with a high-hardness-filler, the measurement revealed decreases in the

hardness with increasing filler content (from 11.8 GPa for YS_0 to 8.7 GPa for YS_{20}). This deterioration in hardness is related to the formation of new Y_2SiO_5, $Y_2Si_2O_7$, and TiO_2 phases. The hardness values for these phases from the literature are 5.3 GPa for Y_2SiO_5 (85), 6.6 GPa for β-$Y_2Si_2O_7$ (86), and 11 GPa for TiO_2 (87), which are all softer than $Y_2Ti_2O_7$. The appearance of these phases in the matrix, and the low density of composites due to the addition of SiC fillers (see Table 3.1) play a decisive role in reducing the total hardness of the composite. Meanwhile, the fracture toughness was enhanced with increased filler content, similar to the $Y_2Ti_2O_7$/Ni composites. When the secondary phases are discretely dispersed in the matrix, as shown in Fig. 10b and Fig. 10e, the cracks induced in the YS_5 composite are shorter and more deflected than those in $Y_2Ti_2O_7$ (Fig. 3.10a and Fig. 3.10d). As a result, toughness was slightly improved from 1.43 MPa.m$^{1/2}$ for monolithic YS_0 to 1.85 MPa.m$^{1/2}$ for YS_5. We consider that the high toughness of SiC (4.6 MPa.m$^{1/2}$) (64), Y_2SiO_5 (1.8 MPa.m$^{1/2}$) (85), and TiO_2 (6.8 MPa.m$^{1/2}$) (87) also contribute to the toughening of the composites. Although these phases are much brittle than nickel (K_{IC} is around 69 MPa.m$^{1/2}$ (88)), the toughening effect of SiC fillers at high concentration is more impressive than that of ductile Ni fillers. The toughness shows a 2.7-fold-increase (1.43 MPa m$^{1/2}$ for YS_0 versus 3.80 MPa m$^{1/2}$ for YS_{20}), in comparison to the above mentioned 2.2-fold-increase of YTO/Ni composites. The remarkably high toughness of high-SiC-content composites is attributed to the network microstructure of the SiC, Y_2SiO_5, and TiO_2 secondary phases. These phases appear as bright contrast domains in the SEM micrographs of Vickers indentations shown in Figure 3.10. The network structure effectively dissipates the fracture energy of cracks propagated from the indentation by bridging and deflection (see Fig. 3.10c and Fig. 3.10f), which hinders crack growth significantly.

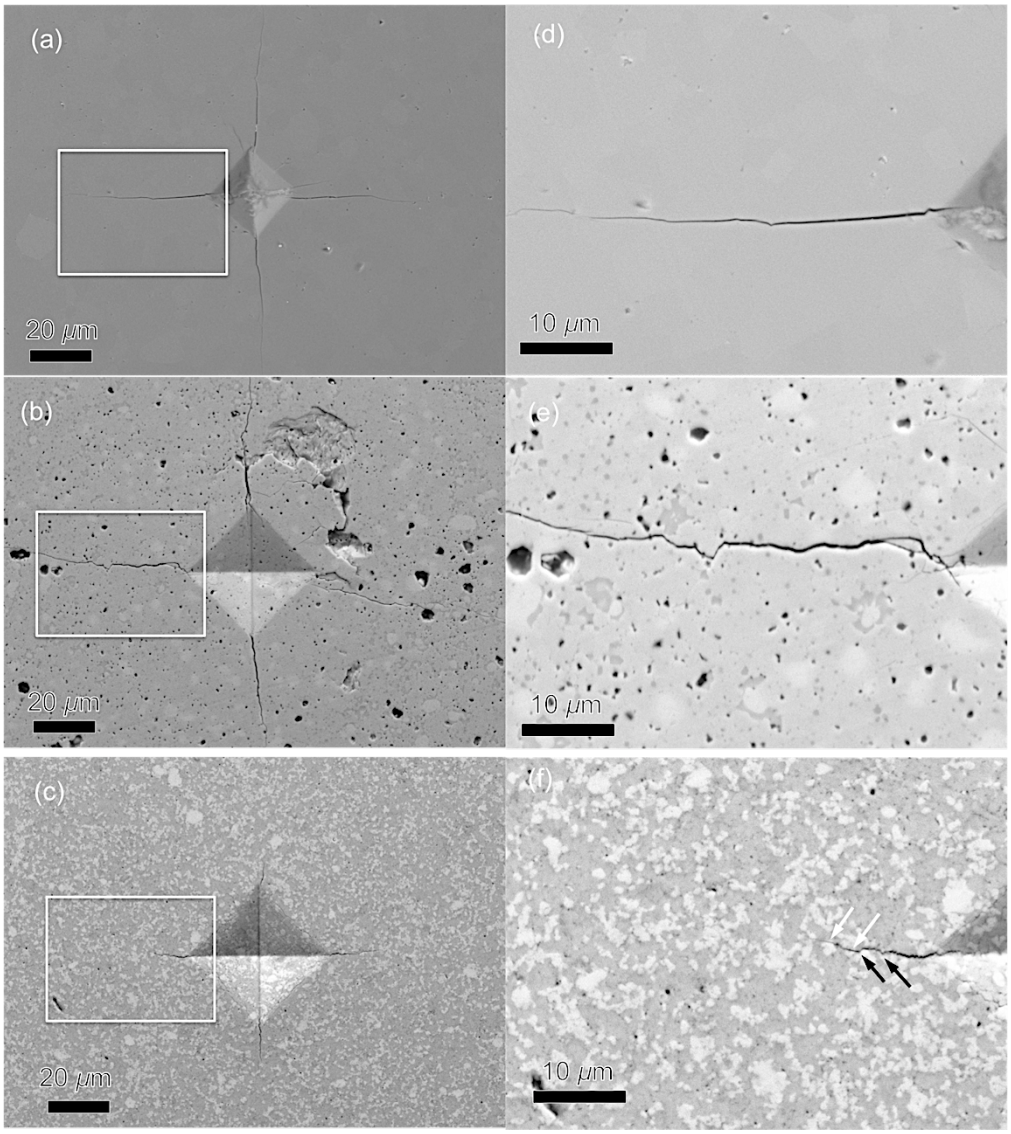

Fig. 3.10. SEM micrographs of Vickers indentations on (a) YS_0, (b) YS_5, and (c) YS_{20} composites surfaces. (d–f) Magnified images of the square regions marked in (a–c), respectively. The white and black arrows in (f) indicate crack bridging and crack deflection, respectively.

3.4. Conclusions

In this chapter, the compatibility of $Y_2Ti_2O_7$ with Ni and SiC, essential materials for gas-turbine-engine blades, was investigated via fabrication and evaluation of the mechanical

properties of $Y_2Ti_2O_7$/Ni and $Y_2Ti_2O_7$/SiC nanocomposites. Following conclusions can be drawn from the obtained results:

(1) $Y_2Ti_2O_7$ has thermal conductivity lower than YSZ. This property together with low thermal expansion coefficient and high temperature stability of $Y_2Ti_2O_7$, suggests that this material are a good candidate material for T/EBC.

(2) $Y_2Ti_2O_7$/Ni nanocomposites were successfully synthesized by a hot-pressing method for the first time. No reaction between $Y_2Ti_2O_7$ and Ni was detected. The Vickers hardness of the $Y_2Ti_2O_7$/Ni composites decreased with an increased filler content, whereas the fracture toughness was improved more than twofold.

(3) Reactions between the $Y_2Ti_2O_7$ matrix and SiC fillers during the sintering process to produce $Y_2Ti_2O_7$/SiC composites led to the formation of Y_2SiO_5 and β-$Y_2Si_2O_7$, the segregation of TiO_2, and the extrusion of SiO_2. It is of interest that, the fracture toughness of the composite was significantly enhanced (nearly threefold) due to the network structures of these secondary phases. This toughening effect is even better than the one induced by ductile Ni fillers.

(4) The improvement in fracture toughness after the incorporation of Ni (SiC) fillers is a good signal indicating the potential of $Y_2Ti_2O_7$ as a candidate for T/EBC, especially in the case of TBC because the $Y_2Ti_2O_7$ was demonstrated that very stable against Ni at elevated temperature.

Chapter 4: Fabrication of functionally graded $Y_2Ti_2O_7$/SiC composites

Abstract:

In this chapter, SiC nanofibers were coated with Ni nanoparticles using solution chemistry routes. The Ni-SiC nanofibers then were dispersed into $Y_2Ti_2O_7$ slurry, which had been prepared by ball-milling $Y_2Ti_2O_7$ powder with polyethyleneimine dispersant in 2-propanol solvent. The slurry was then cast into a polyethylene mold and subjected to a magnetic field. After consolidation, the green body was pressure-less sintered in argon atmosphere. Cross-section observation confirmed that Ni-SiC nanofibers were aligned along the magnetic field direction and convex-concave interface between $Y_2Ti_2O_7$ and SiC were successfully formed.

4.1. Introduction

As mentioned in chapter 1, one of the main challenges of multilayered composites is the delamination caused by the thermal expansion mismatch between the layers. Delamination is the phenomenon occurs in multilayer coating system, in which the upper layer is gradually peeled off from the underneath layer (e.g. substrate, bondcoat, etc.) because of the crack extension at the interface of the two layers. The traditional solution to avoid this phenomenon is to add more intermediate layers, which have moderate values of CTE to lessen the mismatch (23). However, the addition of new layers leads to the increasing weight of the composites, and the more complexity in fabrication. In addition, although being lessened, the CTE mismatch is unavoidable completely when the multilayer structure still exists. In other words, the delamination still occurs. From another point of view, the delamination resistance can be improved when the adhesive interface between the two layers was enhanced (40). Figure 4.1 shows two $Y_2Ti_2O_7$ ceramic discs after detached from the sandwich. It is obviously that the molten Al was stick on the left disc much more stronger than on the right disc, despite the fact that these two discs were sintered at the same condition. This is because the

left disc has rougher surface (polished with 9 μm diamond slurry), and the right disc has smoother surface (polished with 1 μm diamond slurry). In general, a convex concave interface may have better delamination resistance than a flat interface. Figure 4.2a proposes a convex-concave structure of $Y_2Ti_2O_7$/SiC composites that can improve the adhesion at the interface of the two layers.

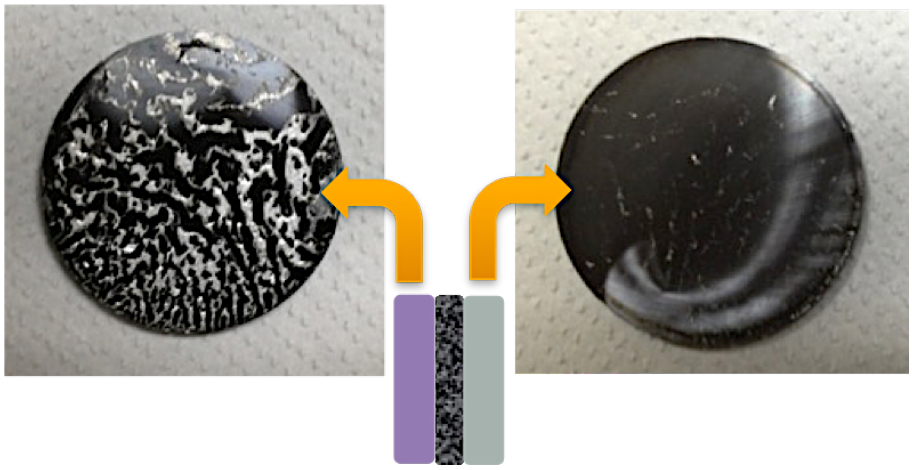

Fig. 4.1. Surfaces of $Y_2Ti_2O_7$ ceramic discs after being detached from the sandwich

The convex-concave interface can be simply fabricated by polishing the interface on sandpaper (Fig. 4.2b), but this method can cause many cracks and deteriorate the mechanical properties of the composite. Another method is usage of sputtering or CVD technique (Fig. 4.2c), however, it is very expensive and extremely complicated in fabrication such a convex-concave interface by this method. It is interesting that particles in a suspension can be attracted and aligned along magnetic field, if those particles are ferromagnetic materials (Fig. 4.2d). This phenomenon has provided an idea for fabricating convex-concave interface structure.

In this chapter, a facile method was developed to fabricate composites with convex-concave interface, by the combination of slurry casting and magnetic field application. In a traditional concept, the composition of a functionally graded composite changes gradually

along a direction, in other words, the composite has gradient distribution of composition. In this convex-concave design of $Y_2Ti_2O_7$/SiC composite, the distribution of the two materials in the interface region also has a gradient distribution, if we consider the composite as an entity. Therefore, in this thesis, the author considers this convex-concave structured composite as a special case of functionally graded composite.

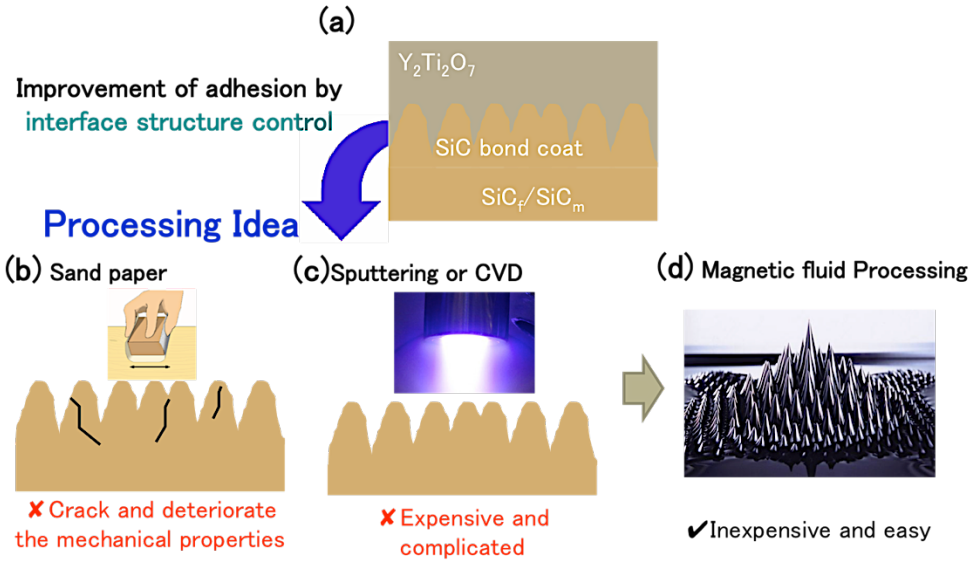

Fig. 4.2. Convex-concave structured composite and the processing idea

4.2. Experimental procedure

4.2.1. Preparation of slurry and application of magnetic field

20 vol % solid content of $Y_2Ti_2O_7$ slurry was prepared by wet ball milling at 150 rpm for 6 h. De-ionized (DI) water, ethyl alcohol, or isopropyl alcohol (IPA) was used as the solvent. Polyethylenimine (PEI) (average molecular weight ca. 10000) (Wako Pure Chemical Industries Ltd., Tokyo, Japan) and 1 mm ZrO_2 balls were used as the dispersant and the milling media, respectively. The dispersant concentrations were 0, 1, or 2 wt % of $Y_2Ti_2O_7$ solid content. The slurry exhibiting the lowest and stable viscosity (Newtonian behavior) then was elutriated to prepare for the casting.

Because SiC is paramagnetic material, they can not be aligned in a magnetic field. Therefore, in this research, the surface of SiC nanofibers (Sigma Aldrich) was coated with Ni nanoparticles by a similar solution chemistry method described in Chapter 3. At first, small amount of nickel nitrate $Ni(NO_3)_2 \cdot 6H_2O$ corresponding to 15 vol% Ni in the final product was mixed with SiC nanofibers and ball-milled in high purity ethanol (99.5%) for 24 h. After being dried overnight at 80 °C, the powder mixture was ground with a mortar and pestle before being calcined in air at 400 °C for 2 h, followed by heat-treatment in 97% Ar + 3% H_2 gas mixture at 800 °C for 2 h. As a result, the surface of SiC nanofibers was attached by nanosized Ni particles.

The Ni-coated SiC nanofibers (Ni-SiC_{nf}) then were introduced into the elutriated slurry. The mixtures were then further sonicated for 15 mins to homogeneously distribute Ni-SiC nanofibers. Subsequently, slurry was poured into cylindrical polyethylene containers (Ø = 25 mm), and subjected to a magnetic field (0.1T or 0.44 T) to be consolidated into green compacts at room temperature. During the consolidation process of slurry into green compact, the magnetic field induced the alignment of Ni particles. The slurry was also poured into another container and consolidated without applying of magnetic field to prepare a reference sample. After the consolidation, the green compacts were removed from magnetic field and dried at 80℃ for 24 h. Then, they were removed from the cylinder and further densified using cold isostatic pressing (CIP) to avoid disturbing the particle orientation. The pressure was 150 MPa and holding time was 5 mins. Finally, the green compacts were pressure-less sintered at 1340 °C for 4 h in an argon (Ar) atmosphere. Figure 4.3 shows the illustration of the experimental setups used for the magnetic field application.

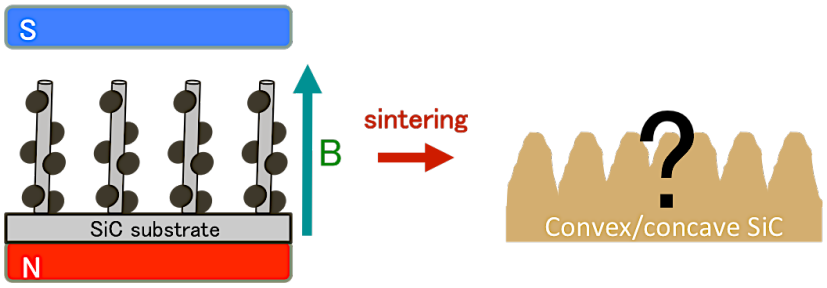

Fig. 4.3. Illustration of the experimental setup used for the magnetic field application

4.2.2. Characterization:

The viscosities of the prepared slurries were measured at room temperature using a rheometer (Physica MCR301; Anton-Paar GmbH, Graz, Austria). The shear rate was changed from 10^{-1} to 10^{2} s^{-1}. The fabricated composites were cut into small specimens to observe the alignment of SiC nanofibers as well as the convex-concave interface of $Y_2Ti_2O_7$ and SiC using scanning electron microscope (SEM). The composition of each layer was investigated using EDS. The specimens were indented by a micro Vickers hardness tester (MVK-H3, Akashi) with different loads (50 and 200 gf) at different positions to evaluate the delamination resistance of the composites (Fig. 4.4).

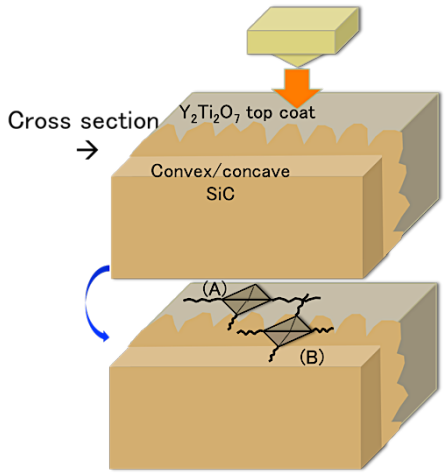

Fig. 4.4. Illustration of the experimental setup used to evaluate delamination resistance

4.3. Results and Discussion:

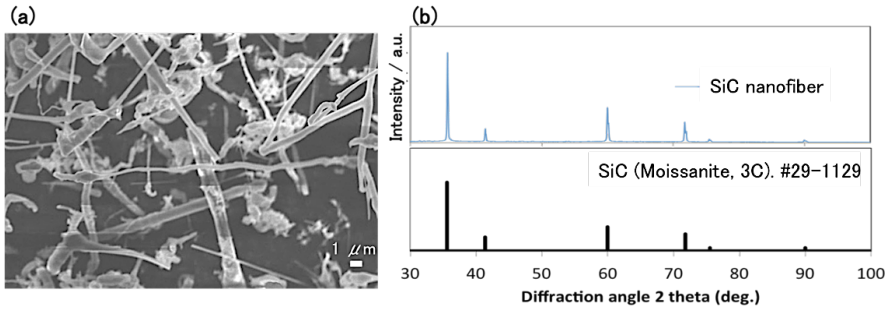

Fig. 4.5 SEM observation (a) and XRD analysis (b) results of as-purchased SiC nanofibers

The SEM micrograph (Fig 4.5a) reveals that the as-purchased fibers have high aspect ratio and a diameter of ca. 500nm. XRD analysis (Fig 4.5b) confirms these nanofibers are beta-SiC (3C) with cubic structure. After the solution chemistry process, SiC fibers have been coated with tiny white particles (Fig. 4.6). As shown in the EDS analysis (Fig. 4.6), the uncoated regions have very low atomic percentage of Ni (ca. 0.6 at%), while the coated regions exhibits much higher atomic percentage of Ni (ca. 11 at%). These results confirm that the tiny white particles are Ni nanoparticles and the coating has been successful.

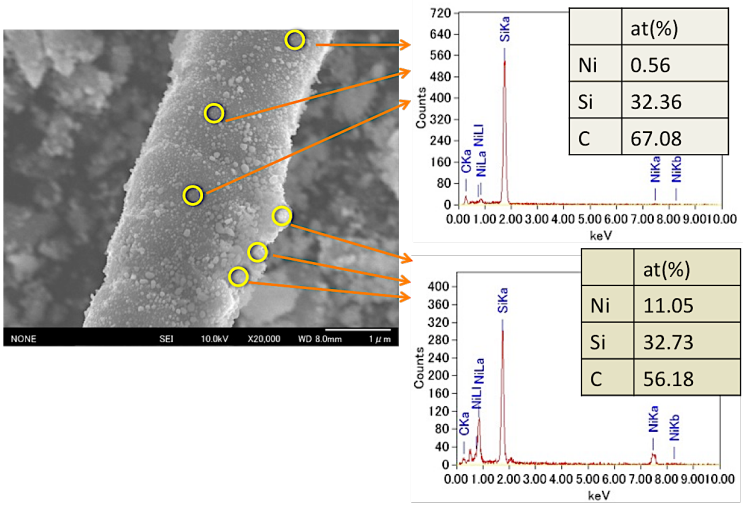

Fig. 4.6. Composition analysis of Ni-coated-SiC fibers using EDS

In slurry casting technique, at first the fluidity of the slurry should be optimized. The optimization can be done through by increasing volume of dispersant, selecting suitable solvent, and reducing particle size. The ball-milling process is often used to reduce the particles size of solid powder. As shown in Fig. 4.7, after 6h of ball-milling, the particle size of $Y_2Ti_2O_7$ reduce significantly and there are very few of $Y_2Ti_2O_7$ agglomerates.

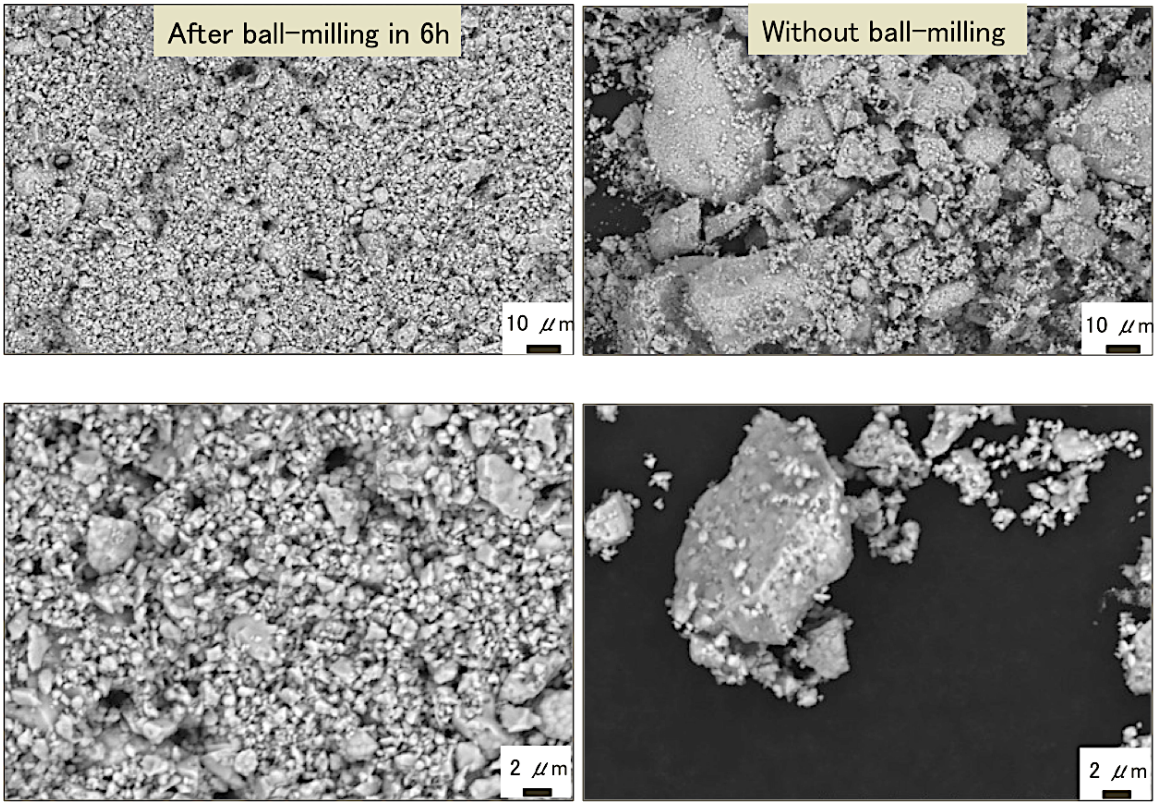

Fig. 4.7. SEM images of $Y_2Ti_2O_7$ powder, with (left) and without (right) ball-milling

In this research, $Y_2Ti_2O_7$ slurry was prepared with DI water, ethyl alcohol, or IPA, which were popular solvents in slurry casting technique. In case of the slurry prepared with DI water, coagulation occurred only 30 mins after the ball-milling (Fig. 4.8a), which means DI water is inappropriate for dispersing $Y_2Ti_2O_7$. The absence of coagulation in the two others slurries, prepared with IPA and ethyl alcohol, indicated that both solvents can well-disperse $Y_2Ti_2O_7$. But the solid $Y_2Ti_2O_7$ was deposited faster in ethyl alcohol than in IPA, as shown in Fig. 4.8b.

Therefore, IPA is selected as the best solvent for slurry casting $Y_2Ti_2O_7$. In another research, Hu et al. (89) also indicated that although IPA had higher viscosity than other solvents, it dispersed nanoparticles and prevented them from re-aggregate better.

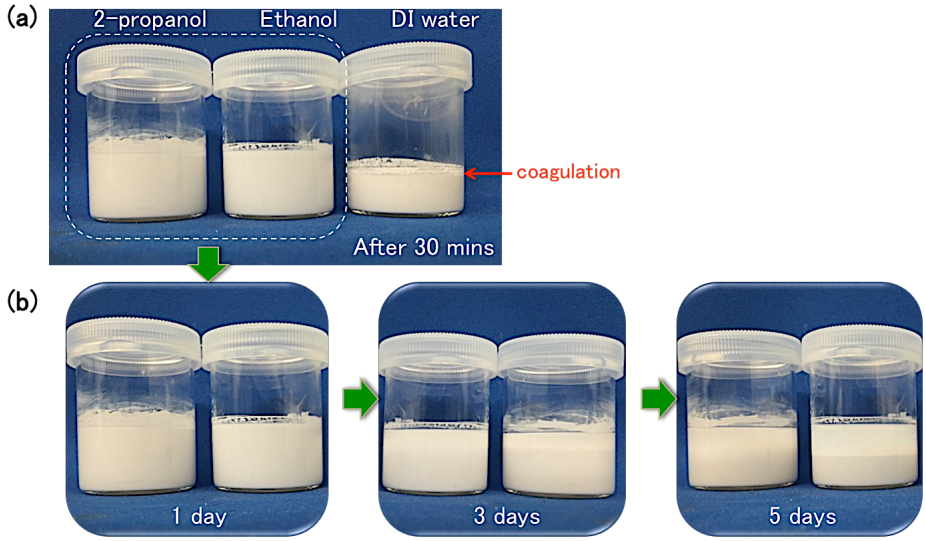

Fig. 4.8. The depositing rate of $Y_2Ti_2O_7$ slurries prepared with different solvent

The effects of solid load, dispersant and ball-milling time on the viscosity of prepared slurries are summarized in Fig. 4.9. The viscosity of slurry decreases with the increasing of dispersant content. Increasing the ball-milling time (5 mins to 6 h) and decreasing the solid content (30 vol % to 20 vol %) also help to reduce the viscosity. Most of slurries have high and unstable viscosity, showing a shear thinning behavior. Only two slurries, prepared with 20% solid load, 2 wt% dispersant, ball-milled in 2 h and in 6 h exhibit Newtonian behavior. The slurry ball-milled in 6h shows lower viscosity, thus it was chosen for casting.

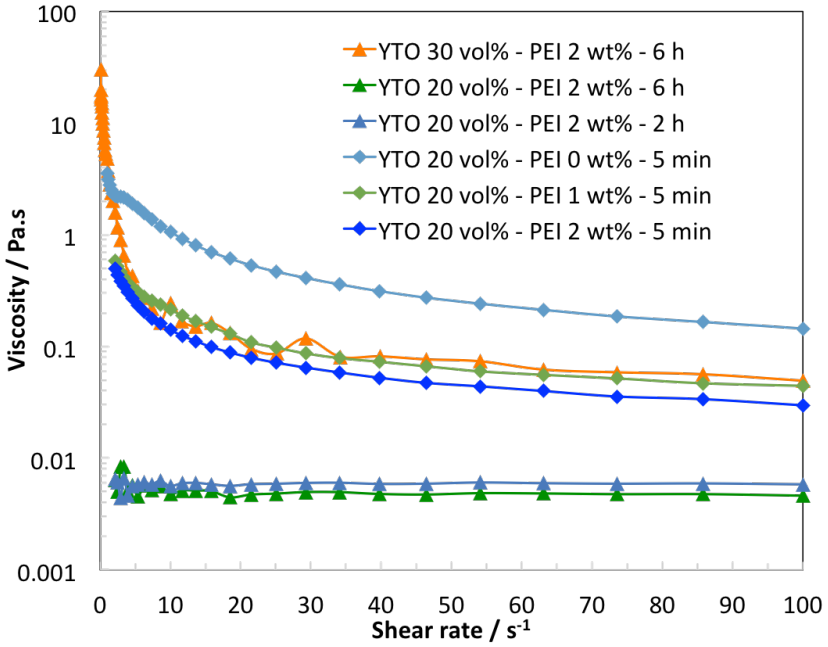

Fig. 4.9. Viscosity of prepared slurries as a function of shear rate

Figure 4.10 shows SEM micrographs of cross-sections of the fabricated composites, applied in 0.1 T and 0.44 T of magnetic fields, respectively. The composites applied in 0.1 T exhibits thinner and longer columns aligning along the magnetic field direction, while the ones applied in 0.44 T shows thicker and shorter columns. It is considered that the denser magnetic field in the case of 0.44 T leads to the formation of the thicker aligned columns.

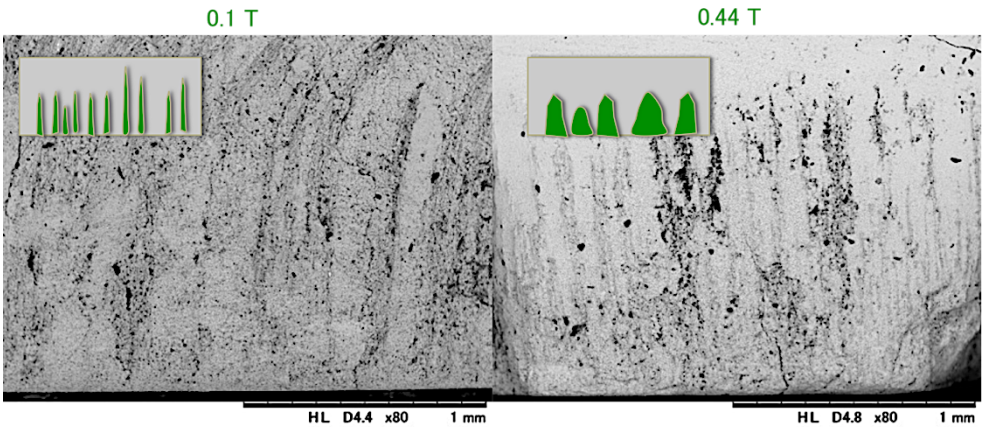

Fig. 4.10. SEM micrographs of composites cross-sections, showing aligned columns.

EDS analysis was conducted to identify the composition of each layer. As shown in Figure 4.11, in top (1) region, the dominant phase is $Y_2Ti_2O_7$, there is a few content of C but no appearance of Si, therefore the signal of C here may come from the carbon tape used to mount the specimen. In the center (2) region, there are appearances of both $Y_2Ti_2O_7$ and SiC. In the bottom region (3), there is almost the appearance of SiC phase. These results confirm that SiC nanofibers has been aligned to form convex concave structures (greater density of SiC at the bottom and lesser density of SiC at the top), and that only a few content of Ni particles attachment are adequate to align SiC fiber under the magnetic field.

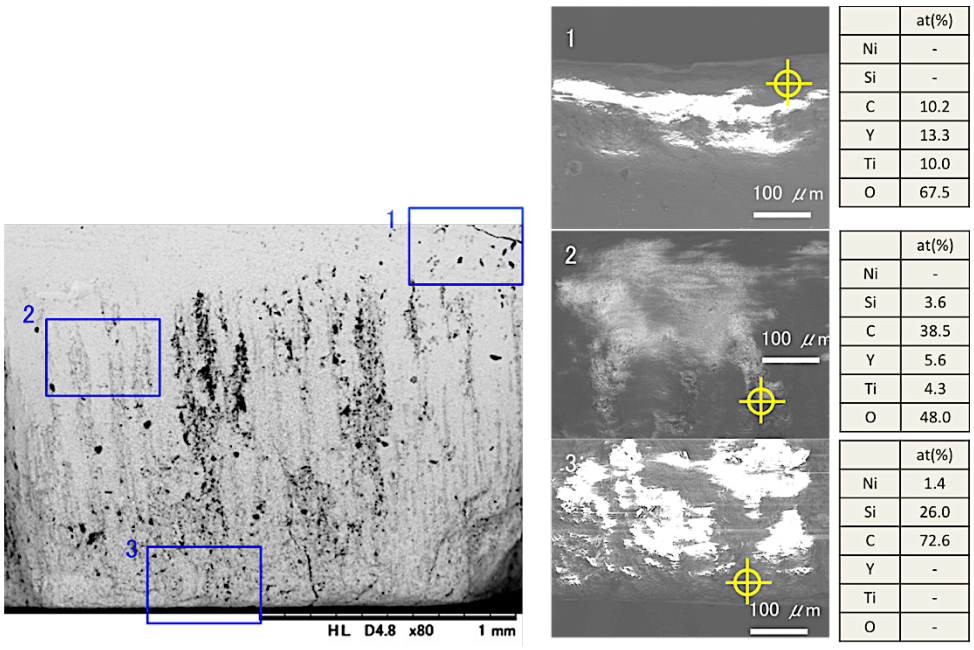

	at(%)
Ni	-
Si	-
C	10.2
Y	13.3
Ti	10.0
O	67.5

	at(%)
Ni	-
Si	3.6
C	38.5
Y	5.6
Ti	4.3
O	48.0

	at(%)
Ni	1.4
Si	26.0
C	72.6
Y	-
Ti	-
O	-

Fig. 4.11. EDS analysis conducted on cross-section of fabricated composites

To investigate the delamination and crack resistance of the fabricated composite, indent Vickers tip was indented onto the cross-section of the specimens, at different positions with different loads. It is though that the crack length in B case may shorter than those of A case. As a result, although the surface was indented with lower load (50 gf), it can be observed that there are some long cracks in the (A) case (Fig. 4.12). In the (B) case, the surface was

indented with higher load but there is no appearance of any cracks. This means the fracture toughness has been improved in the (B) case, thanks to the aligned SiC columns, that can be observed from the SEM micrograph.

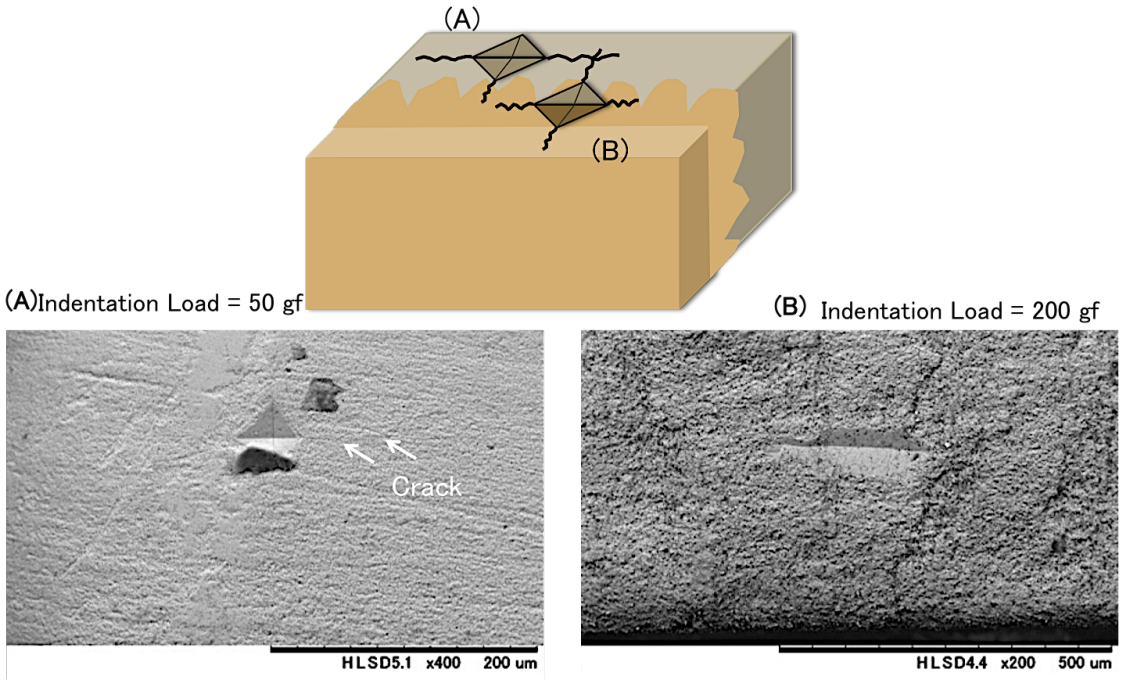

Fig. 4.12. The indentation and crack caused by Vickers tip at (A) and (B) positions

4.4. Conclusions

In this chapter, functionally graded Y_2Ti_2O7/SiC composites were fabricated by casting the composites slurry under a magnetic field inducement. This method is considered to be able to align Ni-SiC fibers along the magnetic field to form convex concave interface between the two layers. From the obtained results, following conclusions can be inferred:

(1) For the first time $Y_2Ti_2O_7$/SiC composites with functionally graded structure were fabricated by a novel technique: a combination of slurry casting and magnetic field inducement. This processing technique is very cheap but was proved to be effective in fabricating functionally graded materials, thus it is highly potential.

(2) There was no crack in the interface between SiC and $Y_2Ti_2O_7$ layers. This suggests that the material has high potential in delamination resistance.

(3) It is a very interesting outcome that the aligned structures seem to improve the fracture toughness of the composites significantly.

Chapter 5: General Conclusions

In chapter 1, the development and role of environmental-resistant ceramic oxides were mentioned. Known ceramic oxides like Al_2O_3, mullite, YSZ, etc. were reviewed and considered are facing of many challenges, therefore it is necessary to find new candidate materials to for environmental-resistant applications. Then, $Y_2Ti_2O_7$ was introduced as a promising material, owing to its high corrosion resistance, phase stability at high temperature, good mechanical properties, low thermal conductivity and thermal expansion coefficient. A new method to fabricate functionally graded composites with convex concave interface between the layers was also proposed.

In chapter 2, $Y_2Ti_2O_7$ ceramic discs were sintered and then employed to fabricate sandwich with aluminum foils by heat treatment at 800°C for 1 h. It is confirmed that the mechanical properties of $Y_2Ti_2O_7$ ceramics can be improved by increasing the sintering pressure (by hot-pressing or HIP) and by minimizing the particle size of the powder. More interestingly, there was no reaction between $Y_2Ti_2O_7$ and molten Al during the process of fabricating the sandwich. Although a few content of molten Al penetrated to the $Y_2Ti_2O_7$ discs via pores existing in the sintered discs, they a very limited and can be reduced significantly by the densification using HIP process. These results suggest that $Y_2Ti_2O_7$ has excellent corrosion resistance against molten metal, and therefor is a promising material for crucible and casting mold.

In chapter 3, thermal conductivity of $Y_2Ti_2O_7$ was measured and confirmed lower than that of YSZ – a widely used material for T/EBC. This property together with its low thermal expansion coefficient and high temperature stability, suggests that $Y_2Ti_2O_7$ are a promising candidate material for T/EBC. In addition, the compatibility of $Y_2Ti_2O_7$ with Ni and SiC,

essential materials for gas-turbine-engine blades, was investigated via fabrication and evaluation of the mechanical properties of $Y_2Ti_2O_7$/Ni and $Y_2Ti_2O_7$/SiC nanocomposites. The fact that $Y_2Ti_2O_7$ was very stable against Ni at elevated temperature, and that the fracture toughness of $Y_2Ti_2O_7$/Ni composites was improved more than twofold after the incorporation of Ni, indicate the great potential of $Y_2Ti_2O_7$ as a material for TBC. Meanwhile, although reactions between the $Y_2Ti_2O_7$ and SiC was detected, the formation of the network structures of the reaction products, Y_2SiO_5, β-$Y_2Si_2O_7$, and TiO_2, remarkably improve the fracture toughness of the composite nearly threefold. This result is considered that can be very useful for designing new EBC.

In chapter 4, a novel method to fabricate $Y_2Ti_2O_7$/SiC composite with convex-concave interface between the two layers was introduced. The method is a combination of slurry casting and magnetic field inducement techniques to align SiC nanofibers within $Y_2Ti_2O_7$ ceramic matrix until the complete consolidation. This processing technique is very cheap but was proved to be effective in fabricating functionally graded materials, thus it is highly potential. In addition, the fact that there was no crack in the interface between SiC and $Y_2Ti_2O_7$ layers, and that the fracture toughness at the interface region of the composites, indicate that this structure has superior delamination resistance.

From the obtained results, $Y_2Ti_2O_7$ has been confirmed that possesses many excellent properties such as high corrosion resistance, relatively high hardness, low thermal conductivity, phase stability at high temperature. Although the fracture toughness of $Y_2Ti_2O_7$ is quite low it can be improved by incorporating with fillers like Ni or SiC. In addition, $Y_2Ti_2O_7$ is proven to be feasible to many processing techniques like sintering, coating, slurry

casting, etc. The Table 5.1 summaries properties of $Y_2Ti_2O_7$ in comparison with other known environmental-resistant materials like Al_2O_3, mullite, ZrO_2, YSZ, etc. In general, it can be concluded that $Y_2Ti_2O_7$ ceramic oxide and its composites are very promising materials, not only for crucible or casting mold, but also for T/EBC, and many other environmental-resistant applications.

Table 5.1. Comparison properties of $Y_2Ti_2O_7$ and other environmental resistant materials

	Fracture toughness	Corrosion resistance	Low thermal conductivity	Phase stability	Delamination resistance	Hardness
Mullite	×	△	○	×	–	△
Alumina	△	△	×	△	–	△
ZrO_2	○	○	○	○	–	△
YSZ	–	–	△	○	–	△
SiC	△	–	×	○	–	○
$Y_2Ti_2O_7$ Previous studies (43, 51)	×	–	–	○	–	△
$Y_2Ti_2O_7$ This work (method)	× → ○ chapter 2 (nanocomposite)	◎ chapter 2	○ chapter 3	○ chapter 3	○ chapter 4 (magnetic processing)	△ → ○ chapter 2 (densification)

Legend: ×: not good, △: good, ○: very good, ◎: extremely good -: not given

(Source: http://acccuratus.com/materials.html)

References

1. Pattnaik S, Karunakar DB, Jha PK. Developments in investment casting process—A review. J Mater Process Technol. 2012 Nov;212(11):2332–48.

2. Schmitt G. Global needs for knowledge dissemination, research, and development in materials deterioration and corrosion control. World Corros Organ N Y. 2009;

3. Guglielmi M. Sol-gel coatings on metals. J Sol-Gel Sci Technol. 1997;8(1-3):443–9.

4. Yan M, Fan Z. Review durability of materials in molten aluminum alloys. J Mater Sci. 2001;36(2):285–95.

5. Yeomans JA, Page TF. Studies of ceramic-liquid metal reaction interfaces. J Mater Sci. 1990;25(5):2312–20.

6. Kim SK, Youn JI, Kim YJ. Rotating cylinder manufacturing method and investment casting of SiCp/AZ91HP magnesium composites. Mater Sci Technol. 2000;16(7-8):769–75.

7. Kim S, Hong T, Kim Y. Evaluation of thermal stability of mold materials for magnesium investment casting. Mater Trans-JIM. 2001;42(3):539–42.

8. Laurent V, Chatain D, Chatillon C, Eustathopoulos N. Wettability of monocrystalline alumina by aluminium between its melting point and 1273 K. Acta Metall. 1988;36(7):1797–803.

9. Fernández B, Almanza JM, Rodríguez JL, Cortes DA, Escobedo JC, Gutiérrez EJ.

Corrosion mechanisms of $Al_2O_3/MgAl_2O_4$ by V_2O_5, NiO, Fe_2O_3 and vanadium slag. Ceram Int. 2011 Dec;37(8):2973–9.

10. Hirata T, Akiyama K, Yamamoto H. Corrosion resistance of Cr_2O_3-Al_2O_3 ceramics by molten sodium sulphate–vanadium pentoxide. J Mater Sci. 2001;36(24):5927–34.

11. Hirata T, Morimoto T, Deguchi A, Uchida N. Corrosion resistance of alumina-chromia ceramic materials against molten slag. Mater Trans. 2002;43(10):2561–7.

12. Cingi C. Mold-metal reactions in magnesium investment castings. [Espoo]: Helsinki University of Technology; 2006.

13. Bathie WW. Fundamentals of Gas Turbines. 2nd ed. Wiley; 1995.

14. Perepezko JH. The hotter the engine, the better. Science. 2009;326(5956):1068–9.

15. Wu J, Wei X, Padture NP, Klemens PG, Gell M, García E, et al. Low-Thermal-Conductivity Rare-Earth Zirconates for Potential Thermal-Barrier-Coating Applications. J Am Ceram Soc. 2002;85(12):3031–5.

16. Zhao H, Yu F, Bennett TD, Wadley HN. Morphology and thermal conductivity of yttria-stabilized zirconia coatings. Acta Mater. 2006;54(19):5195–207.

17. Clarke DR, Oechsner M, Padture NP. Thermal-barrier coatings for more efficient gas-turbine engines. MRS Bull. 2012;37(10):891–8.

18. Cao X, Vassen R, Stoever D. Ceramic materials for thermal barrier coatings. J Eur Ceram Soc. 2004;24(1):1–10.

19. Lee KN, Fox DS, Bansal NP. Rare earth silicate environmental barrier coatings for

SiC/SiC composites and Si_3N_4 ceramics. J Eur Ceram Soc. 2005;25(10):1705–15.

20. Spitsberg I, Steibel J. Thermal and Environmental Barrier Coatings for SiC/SiC CMCs in Aircraft Engine Applications*. Int J Appl Ceram Technol. 2004;1(4):291–301.

21. Fellet M, Rossner W. Ceramic-matrix composites take the heat. MRS Bull. 2015;40(11):916–8.

22. Lee KN, Fox DS, Eldridge JI, Zhu D, Robinson RC, Bansal NP, et al. Upper temperature limit of environmental barrier coatings based on mullite and BSAS. J Am Ceram Soc. 2003;86(8):1299–306.

23. Richards BT, Wadley HN. Plasma spray deposition of tri-layer environmental barrier coatings. J Eur Ceram Soc. 2014;34(12):3069–83.

24. Opila EJ. Oxidation and volatilization of silica formers in water vapor. J Am Ceram Soc. 2003;86(8):1238–48.

25. Lee KN. Key durability issues with mullite-based environmental barrier coatings for Si-based ceramics. In American Society of Mechanical Engineers; 1999. p. V004T02A020–V004T02A020.

26. Lee KN, Miller RA. Development and environmental durability of mullite and mullite/YSZ dual layer coatings for SiC and Si_3N_4 ceramics. Surf Coat Technol. 1996;86:142–8.

27. He M, Hutchinson J, Evans A. Simulation of stresses and delamination in a plasma-sprayed thermal barrier system upon thermal cycling. Mater Sci Eng A. 2003;345(1):172–8.

28. Evans A, Hutchinson J. The mechanics of coating delamination in thermal gradients. Surf Coat Technol. 2007;201(18):7905–16.

29. Lee KN, Fox DS, Eldridge JI, Zhu D, Robinson RC, Bansal NP, et al. Upper temperature limit of environmental barrier coatings based on mullite and BSAS. J Am Ceram Soc. 2003;86(8):1299–306.

30. Lee KN, Fox DS, Bansal NP. Rare earth silicate environmental barrier coatings for SiC/SiC composites and Si_3N_4 ceramics. J Eur Ceram Soc. 2005;25(10):1705–15.

31. Zhou Y, Zhao C, Wang F, Sun Y, Zheng L, Wang X. Theoretical Prediction and Experimental Investigation on the Thermal and Mechanical Properties of Bulk β-Yb2Si2O7. J Am Ceram Soc. 2013;96(12):3891–900.

32. Niihara K. New Design Concept of Structural Ceramics. J Ceram Soc Jpn. 1991;99(1154):974–82.

33. Sekino T, Nakajima T, Ueda S, Niihara K. Reduction and Sintering of a Nickel–Dispersed-Alumina Composite and Its Properties. J Am Ceram Soc. 1997;80(5):1139–48.

34. Chen R, Chiu Y, Tuan W. Toughening alumina with both nickel and zirconia inclusions. J Eur Ceram Soc. 2000;20(12):1901–6.

35. Camargo PHC, Satyanarayana KG, Wypych F. Nanocomposites: synthesis, structure, properties and new application opportunities. Mater Res. 2009;12(1):1–39.

36. Shi X, Xu F, Zhang Z, Dong Y, Tan Y, Wang L, et al. Mechanical properties of hot-pressed Al_2O_3/SiC composites. Mater Sci Eng A. 2010;527(18):4646–9.

37. Koizumi M. FGM activities in Japan. Compos Part B Eng. 1997;28(1):1–4.

38. Elaldi F. Multilayer Ceramic Composite Armor Design and Impact Tests. In: Mechanical Properties and Performance of Engineering Ceramics and Composites VIII. John Wiley & Sons, Inc.; 2013. p. 173–8.

39. Mahamood RM, Akinlabi ET, Shukla M, Pityana S. Functionally graded material: an overview. In Proceedings of the World Congress on Engineering, WCE 2012; 2012.

40. Suzuki T, Matsuzaki R, Todoroki A, Mizutani Y. Crack growth analysis of a composite/adhesive interface toughened by in-mold surface preparation. Int J Adhes Adhes. 2013;42:36–43.

41. Yamashita S, Ohtsuka S, Akasaka N, Ukai S, Ohnuki S. Formation of nanoscale complex oxide particles in mechanically alloyed ferritic steel. Philos Mag Lett. 2004 Jul;84(8):525–9.

42. Klimiankou M, Lindau R, Möslang A. Energy-filtered TEM imaging and EELS study of ODS particles and Argon-filled cavities in ferritic–martensitic steels. Micron. 2005 Jan;36(1):1–8.

43. Ukai S, Mizuta S, Yoshitake T, Okuda T, Fujiwara M, Hagi S, et al. Tube manufacturing and characterization of oxide dispersion strengthened ferritic steels. J Nucl Mater. 2000;283:702–6.

44. Okuda T, Fujiwara M. Dispersion behaviour of oxide particles in mechanically alloyed ODS steel. J Mater Sci Lett. 1995;14(22):1600–3.

45. Kimura Y, Takaki S, Suejima S, Uemori R, Tamehiro H. Ultra Grain Refining and

Decomposition of Oxide during Super-heavy Deformation in Oxide Dispersion Ferritic Stainless Steel Powder. ISIJ Int. 1999;39(2):176–82.

46. Ukai S, Fujiwara M. Perspective of ODS alloys application in nuclear environments. J Nucl Mater. 2002;307:749–57.

47. Uematsu K, Shinozaki K, Sakurai O, Mizutani N, Kato M. Electrical Conductivity of the System Y_2O_3-TiO_2. J Am Ceram Soc. 1979;62(3-4):219–21.

48. Yamaguchi S, Kobayashi K, Abe K, Yamazaki S, Iguchi Y. Electrical conductivity and thermoelectric power measurements of $Y_2Ti_2O_7$. Solid State Ion. 1998;113:393–402.

49. Xiao HY. Electronic Structure Calculations of $A_2Ti_2O_7$ (A = Dy, Ho, and Y). Adv Condens Matter Phys. 2013;2013:1–8.

50. Johnson MB, James DD, Bourque A, Dabkowska HA, Gaulin BD, White MA. Thermal properties of the pyrochlore, $Y_2Ti_2O_7$. J Solid State Chem. 2009 Apr;182(4):725–9.

51. He LF, Shirahata J, Nakayama T, Suzuki T, Suematsu H, Ihara I, et al. Mechanical properties of $Y_2Ti_2O_7$. Scr Mater. 2011 Mar;64(6):548–51.

52. Ewing RC. Nuclear waste disposal—pyrochlore ($A_2B_2O_7$): Nuclear waste form for the immobilization of plutonium and “minor” actinides. J Appl Phys. 2004;95(11):5949.

53. Sickafus K, Minervini L, Grimes R, Valdez J, Ishimaru M, Li F, et al. Radiation tolerance of complex oxides. Science. 2000;289(5480):748–51.

54. Sickafus KE, Matzke H, Hartmann T, Yasuda K, Valdez JA, Chodak III P, et al. Radiation damage effects in zirconia. J Nucl Mater. 1999;274(1):66–77.

55. Matzke H, Kinoshita M. Polygonization and high burnup structure in nuclear fuels. J Nucl Mater. 1997;247:108–15.

56. Lian J, Chen J, Wang L, Ewing R, Farmer J, Boatner L, et al. Radiation-induced amorphization of rare-earth titanate pyrochlores. Phys Rev B. 2003 Oct;68(13).

57. Ukai S, Okuda T, Fujiwara M, Kobayashi T, Mizuta S, Nakashima H. Characterization of High Temperature Creep Properties in Recrystallized 12Cr-ODS Ferritic Steel Claddings. J Nucl Sci Technol. 2002 Aug;39(8):872–9.

58. Yamashita S, Akasaka N, Ohnuki S. Nano-oxide particle stability of 9–12Cr grain morphology modified ODS steels under neutron irradiation. J Nucl Mater. 2004 Aug;329-333:377–81.

59. Stan T, Wu Y, Odette GR, Sickafus KE, Dabkowska HA, Gaulin BD. Fabrication and Characterization of Naturally Selected Epitaxial Fe-{111} $Y_2Ti_2O_7$ Mesoscopic Interfaces: Some Potential Implications to Nano-Oxide Dispersion-Strengthened Steels. Metall Mater Trans A. 2013;44(10):4505–12.

60. Wada T, Kitaoka S, Kashiwagi K. Heat reflecting material, component for molten metal having the same, and coating agent. Japan Fine Ceramics Center; 2013-173180, 2013. p. 1–12.

61. Cernuschi F, Bianchi P, Leoni M, Scardi P. Thermal diffusivity/microstructure relationship in Y-PSZ thermal barrier coatings. J Therm Spray Technol. 1999;8(1):102–9.

62. Pavitra E, Raju G, Yu JS. Solvothermal synthesis and luminescent properties of $Y_2Ti_2O_7$: Eu^{3+} spheres. Phys Status Solidi RRL-Rapid Res Lett. 2013;7(3):224–7.

63. Gill JK, Pandey O, Singh K. Role of sintering temperature on thermal, electrical and structural properties of $Y_2Ti_2O_7$ pyrochlores. Int J Hydrog Energy. 2011;36(22):14943–7.

64. Yamada K, Mohri M. Properties and applications of silicon carbide ceramics. In: Silicon Carbide Ceramics—1. Springer; 1991. p. 13–44.

65. Vassen R, Cao X, Tietz F, Basu D, Stöver D. Zirconates as new materials for thermal barrier coatings. J Am Ceram Soc. 2000;83(8):2023–8.

66. Lutique S, Konings R, Rondinella V, Somers J, Wiss T. The thermal conductivity of $Nd_2Zr_2O_7$ pyrochlore and the thermal behaviour of pyrochlore-based inert matrix fuel. J Alloys Compd. 2003;352(1):1–5.

67. Rigaud M. Corrosion of refractories and ceramics. Uhligs Corros Handb. 2011;51:387.

68. Gogotsi, YG, Lavrenko VA. Corrosion of high-performance ceramics. Springer; 1992.

69. Rice RW. Grain size and porosity dependence of ceramic fracture energy and toughness at 22 °C. J Mater Sci. 1996;31(8):1969–83.

70. Abdul-Aziz A, Abdi F, Bhatt RT, Grady JE. Durability Modeling of Environmental Barrier Coating (EBC) Using Finite Element Based Progressive Failure Analysis. J Ceram. 2014;2014.

71. Niihara K, Kim B-S, Nakayama T, Kusunose T, Nomoto T, Hikasa A, et al. Fabrication of complex-shaped alumina/nickel nanocomposites by gelcasting process. J Eur Ceram Soc. 2004;24(12):3419–25.

72. Levi CG, Hutchinson JW, Vidal-Sétif M-H, Johnson CA. Environmental degradation of

thermal-barrier coatings by molten deposits. MRS Bull. 2012;37(10):932–41.

73. Mouritz AP. 2 - Aerospace materials: past, present and future. In: Introduction to Aerospace Materials [Internet]. Woodhead Publishing; 2012. p. 15–38.

74. Niihara K, Nakahira A, Hirai T. The effect of stoichiometry on mechanical properties of boron carbide. J Am Ceram Soc. 1984;67(1).

75. Langford JI, Wilson A. Scherrer after sixty years: a survey and some new results in the determination of crystallite size. J Appl Crystallogr. 1978;11(2):102–13.

76. Halder N, Wagner C. Analysis of the broadening of powder pattern peaks using variance, integral breadth, and Fourier coefficients of the line profile. In: Advances in X-ray Analysis. Springer; 1966. p. 91–102.

77. Gavrilović TV, Jovanović DJ, Lojpur V, Dramićanin MD. Multifunctional Eu^{3+}-and Er^{3+}/Yb^{3+}-doped $GdVO_4$ nanoparticles synthesized by reverse micelle method. Sci Rep. 2014;4.

78. Jung A, Natter H, Hempelmann R, Lach E. Nanocrystalline alumina dispersed in nanocrystalline nickel: enhanced mechanical properties. J Mater Sci. 2009;44(11):2725–35.

79. Sun X, Yeomans J. Microstructure and fracture toughness of nickel particle toughened alumina matrix composites. J Mater Sci. 1996;31(4):875–80.

80. Liu Y, Zhou J, Shen T. Effect of nano-metal particles on the fracture toughness of metal–ceramic composite. Mater Des. 2013;45:67–71.

81. Czanderna A, Rao CR, Honig J. The anatase-rutile transition. Part 1.—Kinetics of the

transformation of pure anatase. Trans Faraday Soc. 1958;54:1069–73.

82. Cupid DM, Fabrichnaya O, Seifert HJ. Thermodynamic aspects of liquid phase sintering of SiC using Al_2O_3 and Y_2O_3. Int J Mater Res. 2007;98(10):976–86.

83. Levin E, Robbins C, McMurdie H. Phase Diagrams for Ceramists, 1969 supplement. MK Reser Am Ceram Soc Columb OH. 1969;2:107.

84. Levin E, Robbins C, McMurdie H. Phase Diagrams for Ceramists. MK Reser Am Ceram Soc Columb OH. 1964;1:69.

85. Sun Z, Wang J, Li M, Zhou Y. Mechanical properties and damage tolerance of Y_2SiO_5. J Eur Ceram Soc. 2008;28(15):2895–901.

86. Hay RS, Cinibulk MK, Boakye EE, Keller K, Mogilevsky PS, Parthasarathy T, et al. Processing and Testing $Re_2Si_2O_7$ Matrix Composites (Preprint). DTIC Document; 2012.

87. Li J, Forberg S, Hermansson L. Evaluation of the mechanical properties of hot isostatically pressed titania and titania-calcium phosphate composites. Biomaterials. 1991;12(4):438–40.

88. Hohenwarter A, Pippan R. Fracture and fracture toughness of nanopolycrystalline metals produced by severe plastic deformation. Philos Trans R Soc Lond Math Phys Eng Sci. 2015;373(2038):20140366.

89. Hu C, Sakka Y, Tanaka H, Nishimura T, Grasso S. Fabrication of textured Nb4AlC3 ceramic by slip casting in a strong magnetic field and spark plasma sintering. J Am Ceram Soc. 2011;94(2):410–5.

Acknowledgement

I wish to express my greatest gratitude to Associate Professor Tadachika Nakayama at Extreme Energy-Density Research Institute, Nagaoka University of Technology for his kind guidance, invaluable advices and warmhearted encouragement throughout all of this research.

I wish to express the deepest gratitude to Professor Hisayuki Suematsu at Extreme Energy-Density Research Institute, Nagaoka University of Technology for his invaluable suggestions and warmhearted encouragement to complete this thesis.

I wish to express my grateful appreciation to Professor Koichi Niihara, former President of the Nagaoka University of Technology, and former Director of Extreme Energy-Density Research Institute for his invaluable advices and encouragement to complete this research.

I wish to express my grateful appreciation to Associate Professor Tsuneo Suzuki at Extreme Energy-Density Research Institute, Nagaoka University of Technology, for his precious advices and comments during this research.

I wish to express my sincere gratitude to Professor Masatoshi Takeda, Professor Makoto Nanko, Associcate Professor Yukio Miyashita, and Associate Professor Satoshi Tanaka at Nagaoka University of Technology for their precious advices, great discussion, and practical comments to complete this thesis.

I wish to express my sincere gratitude to Professor Weihua Jiang and Assistant Professor Taichi Sugai at Extreme Energy-Density Research Institute for their great support to complete this research.

I wish to express sincere gratitude to Research Professor Hong-Baek Cho at Hanyang University, and former Specially Appointed Associate Professor at Extreme Energy-Density

Research Institute, Nagaoka University of Technology, for his precious advises and encouragement for a long time.

I wish to express my sincere gratitude to Professor Masasuke Takata, Professor Kiyoshi Ohishi, former Directors of Extreme Energy-Density Research Institute, and Professor Yasuhiro Wada, current Director of Extreme Energy-Density Research Institute, for their kindness and great support to complete this research.

I wish to express my sincere gratitude to Technical Assistant Mr. Akio Shida, Secretary Kayoko Watanabe, Secretary Eriko Hasegawa, Secretary Chinami Shiraishi, Secretary Asami Kobayashi, and Secretary Ms. Nana Konishi at Extreme Energy-Density Research Institute of Nagaoka University of Technology for their great support and encouragement during this research.

I wish to express grateful appreciation to Dr. Takeshi Fujihara, Dr. Tomoya Aoba, Dr. Kazuma Suzuki at Extreme Energy-Density Research Institute for their huge scientific and technical supports, as well as for their precious encouragement.

I wish to express grateful appreciation to Research Assistant Noriko Araki, Research Assistant Akira Ishizaki at Extreme Energy-Density Research Institute for their great supports and discussion during this research.

I wish to express grateful appreciation to Dr. Shaifulazuar Bin Rozali, University of Malaya, and former Research Assistant at Extreme Energy-Density Research Institute for his precious assistance and great discussion at the beginning steps of this research.

I wish to thank to all former and current students at Extreme Energy-Density Research Institute, who greatly supported me to complete this research. Especially, great thanks to Mr. Satoshi Amarume, Mr. Hiroya Nakata, Mr. Nguyen Chung Tu, Mr. Shunki Shibaoka, Mr.

Yasunori Sato, Mr. Huynh Tan Minh Triet, Mr. Toshiyuki Endo, Mr. Teruhisa Fukushima, Mr. Huynh Diep Phuoc, Mr. Shun Onzo, Mr. Tsubasa Sakashita, Mr. Hiroyuki Akiyama, Mr. Keishi Awaya, Mr. Do Van Lam, Mr. Masanao Kanno, Mr. Kazuhiro Tamegai, Mr. Soma Sato, Ms. Maria Herrera Salazar, Mr. Hayato Hasuike, Mr. Naoto Matsutani, Ms. Hanan Jawad Al-Sulaiman, and Mr. Genki Onishi for their invaluable assistance, great discussion and encouragement during this research.

I wish to express my sincere appreciation to Dr. Santiago Suarez-Vazquez, Mr. Hironobe Kuribayashi, and Mr. Yoshihiro Nagasawa at Nagaoka University of Technology for their great assistance and discussion in HIP experiment, in thermal properties measurement, and in slurry preparation, respectively, during this research.

I wish to acknowledge the scholarship supported by Ministry of Education, Culture, Sports, Science and Technology (MEXT) and the Grant-in-Aid for Scientific Research from Japan Society for the Promotion of Science (JSPS) during pursuing my PhD program and doing research in Nagaoka University of Technology.

Finally, I wish to express my deepest gratitude to my wife Dao Thi Ngoc Hoang, my family, and my friends, who always support and warmheartedly encourage me to complete this thesis.

Again, I wish to express sincere gratitude to you all.

August 2016

Nguyen Son Thanh

List of Publication

1) S.T. Nguyen, T. Nakayama, H. Suematsu, T. Suzuki, M. Takeda, K. Niihara, "Low thermal conductivity $Y_2Ti_2O_7$ as a candidate material for thermal/environmental barrier coating", *Ceramics International*, vol. 42, no. 9, pp. 11314-11323, Jul 2016

2) H-B. Cho, T. Nakayama, M.T.T. Huynh, S.T. Nguyen, W. Jiang, T. Suzuki, H. Suematsu, K. Niihara, J.H. Shin, Y-H. Choa, "Texture-controlled hybrid materials fabricated using nanosecond technology", *Journal of the Ceramic Society of Japan*, vol. 124, no. 3, pp. 197-202, Mar 2016

3) M.T.T. Huynh, T. Nakayama, A. Kawamoto, S.T. Nguyen, T. Suzuki, H. Suematsu, K. Niihara, H-B. Cho, Y-H. Choa, "Fabrication of stacked-cup carbon nanotube/polymer nanocomposite films with linear controlled percolation routes", *Materials Chemistry and Physics*, vol. 171, pp. 39-44, Mar 2016

4) S.T. Nguyen, T. Nakayama, H. Suematsu, T. Suzuki, M. Nanko, H-B. Cho, M.T.T. Huynh, W. Jiang, K. Niihara, "Synthesis of molten-metal corrosion resistant yttria-based refractory by hot-pressing and densification", *Journal of the European Ceramic Society*, vol. 35, no. 9, pp. 2651–2662, Sep 2015

5) M.T.T. Huynh, H-B. Cho, T. Nakayama, S.T. Nguyen, H. Suematsu, T. Suzuki, W. Jiang, K. Niihara, "Fabrication and Electrical Properties of Cup-Stacked Carbon Nanotubes/Polymer Nanocomposite Films as an Electrode Sensor for Brain-Wave Detection", in Developments in Strategic Materials and Computational Design V: A Collection of Papers Presented at the 38th International Conference on Advanced Ceramics and Composites January 27-31, 2014 Daytona Beach, Florida (eds W.M. Kriven, D. Zhu, K.I. Moon, T.

Hwang, J. Wang, C. Lewinsohn, Y. Zhou), John Wiley & Sons, Inc., Hoboken, NJ, USA, pp. 219-228, Feb 2015

6) S.T. Nguyen, T. Nakayama, S.B. Rozali, H. Suematsu, T. Suzuki, W. Jiang, S. Amarume, L.F. He, K. Niihara, "Developing Yttria-Based Ceramics Having High Liquid Metal Corrosion Resistance", in Advances in Materials Science for Environmental and Energy Technologies III, Volume 250 (eds T. Ohji, J. Matyáš, N.J. Manjooran, G. Pickrell, A. Jitianu), John Wiley & Sons, Inc., Hoboken, NJ, USA, pp. 53-63 (2014), Oct 2014

7) S.T. Nguyen, H-B. Cho, T. Nakayama, M.T.T. Huynh, H. Suematsu, T. Suzuki, W. Jiang, S. Tanaka, Y. Tokoi, K. Niihara, "Linear assembly of oxidized surface treated nanodiamonds in polymer-based nanohybrids by electric field inducement", *Materials Science Forum*, vol. 761, pp. 107-111, Jul 2013

8) H-B. Cho, S.T. Nguyen, T. Nakayama, M.T.T. Huynh, H. Suematsu, T. Suzuki, W. Jiang, S.B. Rozali, Y. Tokoi, Y.H. Park, K. Niihara, "Oxidation of nanodiamonds and modulation of their assembly in polymer-based nanohybrids by field-inducement", *Journal of Materials Science*, vol. 48, no. 12, pp. 4151-4162, Jun 2013

9) H-B. Cho, M.T.T. Huynh, T. Nakayama, S.T. Nguyen, H. Suematsu, T. Suzuki, W. Jiang, S. Tanaka, Y. Tokoi, T. Sekino, K. Niihara, "Densely packed linear assembles of carbon nanotube bundles in polysiloxane-based nanocomposite film", *Journal of Nanomaterials*, vol. 2013, Article ID: 564307: 1-10, Jan 2013

10) H-B. Cho, S.T. Nguyen, T. Nakayama, H. Suematsu, T. Suzuki, W. Jiang, S. Tanaka, B.S. Kim, K. Niihara, "Polyepoxide-based nanohybrid films with self-assembled linear assemblies of nanodiamonds", *Acta Materialia*, vol. 60, no. 20, pp. 7249-7257, Dec 2012

List of International Conference and Presentation

Oral presentation:

1) S.T. Nguyen, T. Nakayama, H. Suematsu, T. Suzuki, S. Tanaka, Y. Nagasawa, K. Niihara, "Fabrication of $Y_2Ti_2O_7$/SiC Functionally Graded Materials by Magnetic Field Application", International Conferences on Modern Materials & Technologies (CIMTEC) 2016, Perugia, Italy, 5-9/6/2016.
2) S.T. Nguyen, T. Nakayama, H. Suematsu, T. Suzuki, M. Takeda, K. Niihara, "Microstructure and Mechanical of $Y_2Ti_2O_7$/SiC nanocomposites", Annual Meeting of The Ceramics Society of Japan 2016, Tokyo, Japan, 14-16/3/2016.
3) S.T. Nguyen, T. Nakayama, H. Suematsu, T. Suzuki, M. Takeda, Y. Nagasawa, S. Tanaka, K. Niihara, "Fabrication of Functionally Graded Composites by Slurry Casting and Magnetic Field Application", The 32nd International Japan-Korea Seminar on Ceramics (JK-Ceramics 32), Nagaoka, Japan, 18-21/11/2015.
4) S.T. Nguyen, T. Nakayama, T. Suzuki, H. Suematsu, M. Nanko, K. Niihara, "Sintering of $Y_2Ti_2O_7$ Ceramics", International Symposium on Hybrid Nano Materials towards Future Industry (HNM 2015), Nagaoka, Japan, 9-11/2/2015.
5) S.T. Nguyen, T. Nakayama, M.T.T. Huynh, T. Suzuki , H. Suematsu, M. Nanko, L.F. He, K. Niihara , "Effect of Densification on Molten-metal Corrosion Resistance of $Y_2Ti_2O_7$ Ceramics", The 5th International Congress on Ceramics (ICC5), Beijing, China, 17-21/8/2014.
6) S.T. Nguyen, T. Nakayama, S.B. Rozali, H. Suematsu, T. Suzuki, W. Jiang, S. Amarume, L.F. He, K. Niihara, "Developing Yttria-Based Ceramics Having High Liquid Metal Corrosion Resistance", Materials Science and Technology 2013

Conference and Exhibition (MS&T' 13), Montreal, Quebec, Canada, 27-31/10/2013.

7) S.T. Nguyen, H-B. Cho, T. Nakayama, M.T.T. Huynh, H. Suematsu, T. Suzuki, W. Jiang, S. Tanaka, Y. Tokoi, K. Niihara, "Linear Assembly of Oxidized Surface Treated Nanodiamond in Polymer-based Nanohybrids by Electric Field Inducement", The 14th International Symposium on Eco-Materials Processing and Design (ISEPD 2013), Kagoshima, Japan, 15-18/1/2013.

Poster presentation:

1) Nguyen Thanh Son, 中山忠親, Shaifulazuar Bin Rozali, Huynh Tan Minh Triet, 末松久之, 鈴木常生, 江偉華、He Lingfeng, 新原晧一, "イッテリア系セラミックスの焼結プロセスの最適化と熔融金属耐食性評価", 平成 25 年度日本セラミックス協会東北北海道支部研究発表会, 長岡, 24-25/10/2013.

2) S.T. Nguyen, H-B. Cho, T. Nakayama, H. Suematsu, T. Suzuki, W. Jiang, S. Tanaka, K. Niihara, "Epoxy-based Nanocomposite Films with Self-assembled Linear Assemblies of Nanodiamonds", The CJK 2012 Seminar and Spring Workshop, Gyeongju, Korea, 8-12/3/2012.